Quantitative determination of the structures of Bi and Sb thin films grown on Si(lll) and Ge(lll) surfaces
by Kejia Wan

A thesis submitted in partial fulfillment of the requirements for the degree of Doctor of Philosophy in Physics
Montana State University


Abstract:
ABSTRACT The modification of metal-semiconductor interface structures is a very interesting topic, and the geometric structure of such surfaces is a central issue in semiconductor physics. An entire experimental system containing low energy electron diffraction, Auger electron spectroscopy and thin film sample preparation and characterization apparatus has been developed. The computer program for the theoretical analysis of LEED I-V curves has been established. The surface reconstructions of semiconductor Si(111) and Ge(111) due to the adsorption of column-V metal atoms such as Bi and Sb have been studied by this technique. The initial epitaxial growth process and the ordering phenomena were studied as a function of overlayer coverage and deposition conditions.

For the Bi/Si(l 11) system, our experiments show that two equilibrium phases are formed in the growth process, each displaying a (√3x√3)-R30&deg, LEED symmetry: an α-phase occurring at 1/3 ML Bi coverage and substrate temperature of 360° C, and a p-phase at 1 ML and 300°C For the Bi/Ge(111) system, only one (√3x√3) phase was obtained at the 1/3 ML coverage and 380°C substrate temperature. For Sb overlayers, the Si(111) surface exhibits a series of phases with the (√3x√3) structure being the most stable, which appears at 1 ML coverage and 550°C substrate temperature. In contrast, for the Ge(111) substrate, only the ordered (1x1) structure was observed at an Sb coverage of 1 ML and thermal annealing to 380&degC.

Quantitative structural information for each system was determined by multiple scattering analysis of I-V curves. The analysis is facilitated by comparing LEED intensity data measured for each phase with calculated values using appropriate structural models.

For the (√3x√3) surfaces, the T4 geometry for the 1/3 ML case and a timer geometry for the 1 ML case are found to be the best models, while substitution model is responsible for the 1 ML (1x1) surface. The detailed atomic coordinates have been determined for each system.

The surface reconstructions of the above (111) surfaces are discussed in terms of the atomic size effect and chemical bonding nature of the adsorbate and substrate. An understanding of the atomic geometry of the epitaxial overlayers is needed to describe more fully the adatom-induced surface reconstruction. The results could in principle be useful in understanding the origin of the adatom-induced surface reconstruction, and could be important in conjunction with structural studies based on calculations of the total energy versus distortion parameters. The method established from this thesis can eventually be applied to study MBE samples.

# QUANTITATIVE DETERMINATION OF THE STRUCTURES OF Bi AND Sb THIN FILMS GROWN ON Si(111) AND Ge(111) SURFACES

by

Kejia Wan

A thesis submitted in partial fulfillment
of the requirements for the degree

of

Doctor of Philosophy

in

Physics

MONTANA STATE UNIVERSITY
Bozeman, Montana

July, 1991

APPROVAL

of a thesis submitted by

Kejia Wan

This thesis has been read by each member of the thesis committee and has been found to be satisfactory regarding content, English usage, format, citations, bibliographic style, and consistency, and is ready for submission to the College of Graduate Studies.

July 15, 1991
Date

Chairperson, Graduate Committee

Approved for the Major Department

July 15, 1991
Date

Head, Major Department

Approved for the College of Graduate Studies

July 19, 1991
Date

Graduate Dean

## STATEMENT OF PERMISSION TO USE

In presenting this thesis in partial fulfillment of the requirements for a doctoral degree at Montana State University, I agree that the Library shall make it available to borrowers under rules of the Library. I further agree that copying of this thesis is allowable only for scholarly purposes, consistent with "fair use" as prescribed in the U. S. Copyright law. Requests for extensive copying or reproduction of this thesis should be referred to University Microfilms International, 300 North Zeeb Road, Ann Arbor, Michigan 48106, to whom I have granted "the exclusive right to reproduce and distribute copies of the dissertation in and from microfilm and the right to reproduce and distribute by abstract in any format."

Signature Kejia Wan

Date July 7, 1991

# ACKNOWLEDGMENTS

The author owes a special debt of gratitude to some individuals who provided thoughtful advice and encouragement in carrying out the work performed for this thesis. Foremost, the author wishes to thank his two advisors, Dr. W. K. Ford, for his guidance and unlimited advice during all stages of this work; Dr. J. C. Hermanson, for his stimulating discussion, his kindness, and his critical reading of my scientific papers including this thesis.

The author also acknowledges Dr. T. Guo for his important guidance, helpful discussion, and technical assistance. Special thanks go to G. J. Lapeyre, J. Anderson, R. J. Smith, J. Carlsten, A. Eguiluz, and R. T. Robiscoe for their support and advice.

Thanks are due to the staff and fellow graduate students in the Physics Department, M. S. U.

Finally, he wishes to dedicate all his accomplishments to his wife and parents for their spiritual encouragement and support over a number of years.

TABLE OF CONTENTS

TABLE OF CONTENTS - Continued

# LIST OF TABLES

# LIST OF FIGURES

LIST OF FIGURES - Continued

LIST OF FIGURES - Continued

# ABSTRACT

The modification of metal-semiconductor interface structures is a very interesting topic, and the geometric structure of such surfaces is a central issue in semiconductor physics. An entire experimental system containing low energy electron diffraction, Auger electron spectroscopy and thin film sample preparation and characterization apparatus has been developed. The computer program for the theoretical analysis of LEED I-V curves has been established. The surface reconstructions of semiconductor Si(111) and Ge(111) due to the adsorption of column-V metal atoms such as Bi and Sb have been studied by this technique. The initial epitaxial growth process and the ordering phenomena were studied as a function of overlayer coverage and deposition conditions.

For the Bi/Si(111) system, our experiments show that two equilibrium phases are formed in the growth process, each displaying a $(\sqrt{3}\times\sqrt{3})$-R30° LEED symmetry: an $\alpha$-phase occurring at 1/3 ML Bi coverage and substrate temperature of 360° C, and a $\beta$-phase at 1 ML and 300 °C. For the Bi/Ge(111) system, only one $(\sqrt{3}\times\sqrt{3})$ phase was obtained at the 1/3 ML coverage and 380 °C substrate temperature. For Sb overlayers, the Si(111) surface exhibits a series of phases with the $(\sqrt{3}\times\sqrt{3})$ structure being the most stable, which appears at 1 ML coverage and 550 °C substrate temperature. In contrast, for the Ge(111) substrate, only the ordered (1×1) structure was observed at an Sb coverage of 1 ML and thermal annealing to 380 °C.

Quantitative structural information for each system was determined by multiple scattering analysis of I-V curves. The analysis is facilitated by comparing LEED intensity data measured for each phase with calculated values using appropriate structural models. For the $(\sqrt{3}\times\sqrt{3})$ surfaces, the $T_4$ geometry for the 1/3 ML case and a trimer geometry for the 1 ML case are found to be the best models, while substitution model is responsible for the 1 ML (1×1) surface. The detailed atomic coordinates have been determined for each system.

The surface reconstructions of the above (111) surfaces are discussed in terms of the atomic size effect and chemical bonding nature of the adsorbate and substrate. An understanding of the atomic geometry of the epitaxial overlayers is needed to describe more fully the adatom-induced surface reconstruction. The results could in principle be useful in understanding the origin of the adatom-induced surface reconstruction, and could be important in conjunction with structural studies based on calculations of the total energy versus distortion parameters. The method established from this thesis can eventually be applied to study MBE samples.

# CHAPTER 1

## INTRODUCTION

Semiconductor physics is closely related to the development of semiconductor technology. The demand to improve device performance requires the understanding of physical processes in semiconductor material. On the other hand, the rapid development in modern technology has made it possible to produce higher-quality semiconductor devices. Since devices have reached a high level of integration such that surface and interface effects play an important role in determining the characteristics of performance, the study of semiconductor surfaces is one of the major efforts in surface science.[1]

During the past decade, nonequilibrium techniques have been developed for the study of electronic and geometric properties of semiconductor surfaces. Electronic properties near the surface and interface region, such as Schottky barrier formation and Fermi level pinning, are of great practical interest in the manufacture of microelectronics devices. However, a more fundamental, or more microscopic, understanding of these properties depends on knowing the atomic structure of such surfaces. The change in atomic geometry at a surface or interface relative to the bulk involves a variety of factors, including changes in surface work function, the introduction of surface electronic states, vibrational modes, surface strain fields, and a wide range of chemisorption and heterogeneous catalytic phenomena. Therefore, the description of surface electronic properties is greatly improved if the surface atomic structure is known.

Geometric structures with atomic dimensions give rise to new phenomena resulting from quantum-mechanical effects, e.g., low- energy electron diffraction (LEED).[2] Layered structures with a periodicity of a few atomic layers result in coherent behavior for long-range bonding such as ordered interfaces in metal-semiconductor systems. Studies of the geometric structure of metal-semiconductor interfaces have led to significant advances in our basic understanding of the physics of materials as well as to important new technologies. Two aspects of surface structural determination have been investigated extensively by both experiment and theory: the atomic geometries of semiconductor surfaces and interfaces, and the character of the chemical bond between atomic species at surfaces and interfaces. These two issues are emphasized in this thesis. To date, silicon is the most common material in semiconductor technology, and along with germanium and GaAs, is one of the three most important semiconductors.[3]

Much effort has been devoted to the study of the morphology and growth characteristics of metal films on Si, Ge and GaAs, especially films of column-III and column-V elements on Si and Ge. Bismuth and antimony exhibit some interesting properties in connection with metallization in Si device technology.[4] In the studies of metal-III-V semiconductor contacts, bismuth and antimony are found to be among the very few metals that form ordered monolayers on III-V(110) semiconductor surfaces.[5] They exhibit adsorption size effects, indicating that two-dimensional island formation below 1 ML, and interesting surface bonding properties.[6] Thus, both bismuth and antimony adsorption have attracted great interest. In this thesis, we use low-energy electron diffraction (LEED) and Auger spectroscopy (AES) to study Bi and Sb epitaxy on Si(111) and Ge(111) surfaces. This study serves to characterize the types of overlayer formation that occur for column-V atoms on Si and Ge substrates.[7,8] One main thrust of this thesis is to categorize the growth and ordering characteristics according to the atomic size of adatom

and substrate and the chemical nature of their bonding, and to emphasize the differences we observe in the epitaxial behavior of these elements.

When metal atoms (or molecules) are adsorbed onto a semiconductor surface, the adsorbates can be trapped in a potential energy well on the surface. If the surface exhibits long-range two-dimensional periodicity, ordered adlayers can result from the interactions between adsorbate atoms and from the site-dependent interactions between adparticles and substrate. Extensive adsorption studies have been carried out on Si(111) and Ge(111) substrates for the past decade. The adsorption of metal overlayers in the submonolayer range on Si or Ge(111) surfaces can result in surface superstructures with a variety of phases. Among those phases, the ordered $(\sqrt{3}\times\sqrt{3})R30°$ reconstruction is the most frequently observed structure. This reconstruction often appears when column III (Al, Ga, In)[9~11], column IV (Sn,Pb)[12,13], or column V (Sb, Bi)[14,15] atoms are adsorbed on clean Si(111) or Ge(111) surfaces. Some other metals such as Ag and Au also induce this reconstruction. The coverage of the metal films may be 1/3 to 4/3 monolayers depending on the individual group. Models of the $(\sqrt{3}\times\sqrt{3})$ reconstruction have been proposed on the basis of surface total-energy calculations or experimental observations for coverages of 1/3, 2/3, 1, and 4/3 monolayers.[16-18,13] On the other hand, As induces a (1×1) structure on both Si and Ge(111) surfaces.[19,20]

The physical origin of adatom-induced surface reconstruction has previously been studied in terms of the surface total energy.[21,22] An ideal bulk-terminated (111) surface with all atoms located at their ideal bulk positions is not physically realized since it is not at the surface-free-energy minimum, because of the existence of dangling bonds, which are energetically costly. Column-III and column-V adatoms on (111) surfaces saturate the surface dangling bonds, lowering the surface energy. This behavior is described in terms of the chemical bonding between the adsorbate and substrate atoms. Column-III (Al, Ga, In) adatoms induce a $(\sqrt{3}\times\sqrt{3})$ reconstruction on the Si(111) surfaces. The adatom is

believed to be positioned in either the filled site above the second layer Si atoms ($T_4$) or in the hollow site above the fourth layer Si atoms ($H_3$), both sites are energetically stable: three substrate dangling bonds can be passivated by one adsorbate atom in an $sp^3$ bonding geometry.[21]

Column-V As overlayers produce a (1×1) surface unit cell on both Si(111) and Ge(111) surfaces. The As atom has been shown to substitute for the top-most substrate atom to achieve the optimal bonding configuration of both substrate atoms and As atoms: tetrahedral coordination with $sp^3$ hybridized bonding orbitals for the substrate atoms and $p^3$ three-fold bonding for the As atoms. Antimony and bismuth adatoms, by contrast, can induce a complex phase diagram including a ($\sqrt{3}\times\sqrt{3}$) structure. The structural phases depend on the adatom coverage and the thermal environment. Recent structural studies have demonstrated that the ($\sqrt{3}\times\sqrt{3}$) surface reconstruction has trimer adatoms in each ($\sqrt{3}\times\sqrt{3}$) site.[18] The center of the trimer could be located at either the $T_4$ or the $H_3$ site. To date it has not been possible, however, to obtain conclusive experimental evidence for either geometry, and details of the atomic positions remain unknown.

Among the several techniques for locating atoms at surfaces, low-energy electron diffraction (LEED) is still a powerful tool, though other techniques like photoelectron diffraction and electron holography are advancing rapidly.[23] LEED has been applied successfully to a number of metal and semiconductor surfaces.[24] The purpose of this thesis is to accomplish a complete LEED analysis using both experiment and calculation, in order to investigate systematically the structure of the column-V elements adsorbed on Si(111) and Ge(111) substrates. The results could in principle be useful in understanding the origin of the adatom-induced surface reconstructions, and could be important in conjunction with structural studies based on calculations of the total energy versus distortion parameters.

The thesis is organized as follows. Descriptions of surface analysis techniques we used and the experimental set-up, with emphasis on LEED, are given in Chapter 2. The experimental procedures are also discussed there. In Chapter 3, the dynamical LEED theory is reviewed in order to give the basic picture and appropriate physical ingredients for dealing with the calculation of diffraction intensity of the scattered electron beam. The more rigorous general quantum mechanical derivation can be found in the literature. Chapter 4 describes the computational method and computer program used to do LEED intensity analysis; the program is based on the theoretical treatment described in Chapter 3. The studies of Sb, Bi adsorbed on Si(111) and Ge(111) are presented in Chapters 5 and 6, respectively. Chapter 7 presents a comprehensive discussion and summary.

The work in this thesis was initiated by a desire to study the reconstructions of the MBE-grown GaAs surface. The experimental apparatus is compatible with the MBE growth system in the CRISS laboratory in the Physics Department. The computer program can deal with the reconstructions of GaAs(111) surfaces, as well as the (100) surface with some modification. Thus, the method established in this thesis can eventually be applied to study MBE-grown samples.

# CHAPTER 2

# EXPERIMENTAL METHOD AND TECHNIQUES

In the study of the geometric structure of semiconductor surfaces, it is important to understand the experimental facilities, the analytical techniques, and the procedure used in the experiments. Low energy electron diffraction (LEED) and Auger electron spectroscopy (AES) are used to study metallic thin films grown on Si and Ge surfaces. In this chapter, the experimental techniques, the ultra high vacuum chamber, and the instrumentation used in our work are described.

## Surface Crystallography and Low Energy Electron Diffraction

Since a full description of the LEED technique can be found in a number of publications,[24,25] only some basic concepts and methods related to the thesis work are discussed here.

### Surface Classification

The classification and description of the geometric structure of bulk crystalline materials is based on the language of crystallography. Many properties of solids are intimately related to the special symmetry properties of those materials. While a solid surface is intrinsically different from a crystalline solid, in that the three-dimensional periodicity of the structure is reduced to two, the atomic arrangement retains two-

dimensional periodicity parallel to the surface, and this periodicity is an important factor in determining some of the properties of the surface. In particular, periodicity is essential allowing electron diffraction techniques to provide information on the structure of the surface.[24] Thus, a proper understanding of surface crystallography is necessary if one wishes to understand the LEED technique.

By surface geometric structure we mean the atomic geometry of the solid in the vicinity of the surface. The surface can be thought of as a substrate which is bulk-like plus the few atomic layers near the surface, which may be deformed relative to bulk layers. For example, it is common that surface relaxation (displacements perpendicular to the surface) and surface reconstruction (displacements parallel to the surface) occur. Surface relaxation and reconstruction involve either the topmost atom strain due to the breaking of three-dimensionality, or involve foreign atom adsorption, called adatoms in both cases. We will use the term overlayer structure to describe those layers of the surface. Evidently, for ordered surfaces, the periodicity of the overlayer structure is frequently in registry with the substrate periodicity, an important factor in our further discussion. The surface symmetry is characterized by its associated unit mesh which must be consistent with one of the 14 Bravais space lattices. Full descriptions of the various Bravais lattices can be found in the literature.[25] There are five possible distinct two-dimensional Bravais lattices, which are shown in Fig. 1; $\mathbf{a}_1$ and $\mathbf{a}_2$ are primitive translation vectors defining the surface unit mesh, and are generally selected to form the smallest possible parallelogram which preserves the surface symmetries.

In discussing the overlayer structure it is helpful to use a notation which minimizes ambiguities. There are two schemes to relate overlayer structure to that of the underlying substrate. One scheme proposed by Park and Madden (1968) involves a simple vectorial construction,[26] which relates the substrate primitive translation vectors ($\mathbf{a}_1$, $\mathbf{a}_2$) to those of the overlayer ($\mathbf{b}_1$, $\mathbf{b}_2$) with transformation matrix $\boldsymbol{G}$, such that

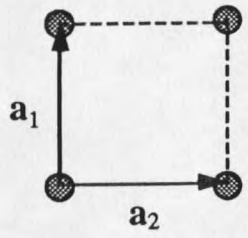


Square

$a_1 = a_2$

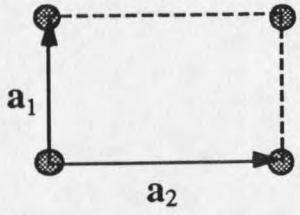


Primitive Rectangular

$a_1 \neq a_2$

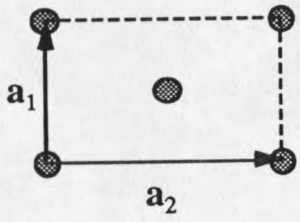


Centered Rectangular

$a_1 \neq a_2$

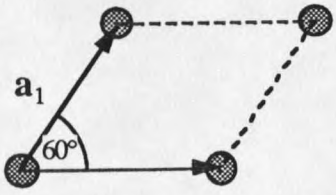


Hexagonal

$a_1 = a_2$

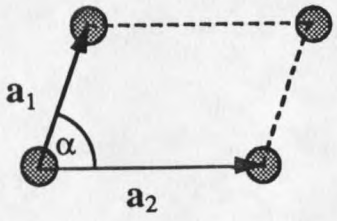


Oblique

$a_1 \neq a_2$

$\alpha \neq 90°$

Fig. 1: The five types of two-dimensional Bravais lattices

$$\mathbf{b}_1 = G11\ \mathbf{a}_1 + G12\ \mathbf{a}_2$$

$$\mathbf{b}_2 = G21\ \mathbf{a}_1 + G22\ \mathbf{a}_2$$

or

$$(\mathbf{b}_1, \mathbf{b}_2) = G\ (\mathbf{a}_1, \mathbf{a}_2) \qquad (2.1)$$

The advantage of this notation is that, because the area of the substrate unit mesh is given by $|\mathbf{a}_1 \times \mathbf{a}_2|$, the determinant of $G$ is simply the ratio of the areas of the two meshes and provides a convenient classification system for the type of overlayer structure. When all components of $G$ are integers, the overlayer structure is called *simple* and the adatom mesh has translation symmetry elements in common with the surface as a whole; if $G$ contains both integers and rational numbers, the overlayer structure is referred to as a *coincidence* structure and the adatom mesh and substrate mesh come into coincidence at regular intervals. When $G$ contains irrational numbers, the overlayer structure is called *incoherent* or *incommensurate*. A disadvantage of this notation is that it doesn't provide an intuitive picture of what the structure looks like.

A more convenient notation for overlayer structure suggested by Wood(1964) is more widely used.[27] In this case the notation defines the ratio of the lengths of the surface and substrate meshes, together with the angle through which one mesh must be rotated to align the two pairs of primitive translation vectors. In this notation if adsorbate A on the {hkl} surface of material *X* causes the formation of a structure having primitive translation vectors of length $|\mathbf{b}_1| = p|\mathbf{a}_1|$ and $|\mathbf{b}_2| = q|\mathbf{a}_2|$ with a unit mesh rotation of $\phi$ the structure is referred to as *X* {hkl}-p×q - R$\phi$°-*A*. Note that the surface unit mesh is labelled as either centered (*c* ), or primitive (*p* ). In a centered unit mesh a lattice point is found in the center of the surface unit mesh. This method is simple and applicable to a large number of structures, including the III-V(110)-(1×1,1×2,1×3)-(Bi, Sb) system we studied

previously[6] and the Si, Ge(111)-$\sqrt{3}$x$\sqrt{3}$-(Bi,Sb) systems studied here. Using $\boldsymbol{G}$ matrix notation, the above structures can be expressed as $\begin{pmatrix} 1 & 0 \\ 0 & 1 \end{pmatrix}$, $\begin{pmatrix} 1 & 0 \\ 0 & 2 \end{pmatrix}$, $\begin{pmatrix} 1 & 0 \\ 0 & 3 \end{pmatrix}$, and $\begin{pmatrix} 1/3 & 0 \\ 0 & 1/3 \end{pmatrix}$, respectively. As an example, the atomic arrangement and the LEED pattern of a ($\sqrt{3}\times\sqrt{3}$) structure with this scheme are presented in Fig. 2.

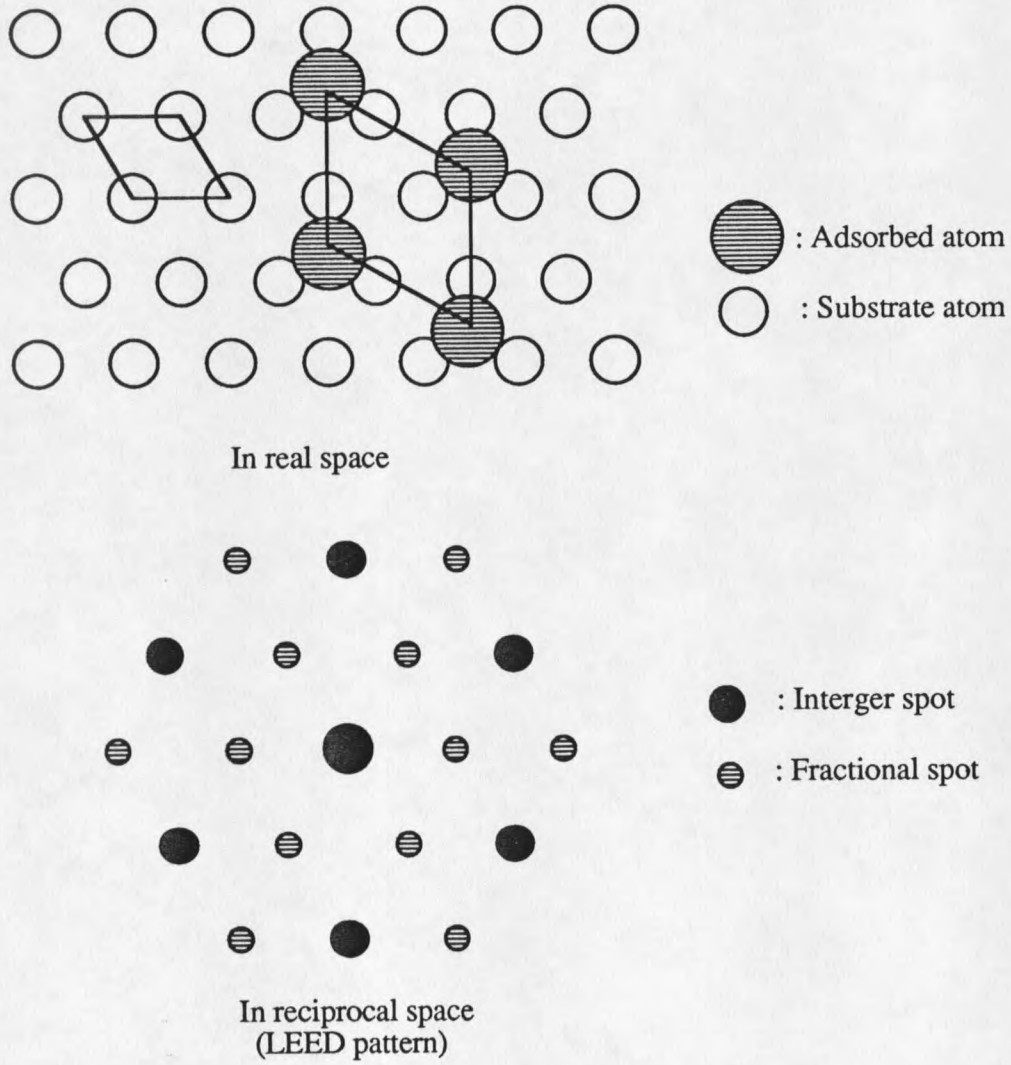


Fig. 2: The ($\sqrt{3}\times\sqrt{3}$) structure in reciprocal space and possible atomic arrangement in real space.

For every two-dimensional lattice, there exists a corresponding reciprocal lattice whose primitive vectors, ($\mathbf{a}_1^*$, $\mathbf{a}_2^*$) satisfy

$$\mathbf{a}_i \cdot \mathbf{a}_j^* = 2\,\pi\,\delta_{ij} \qquad (2.2)$$

Therefore, the ($\mathbf{a}_1^*$, $\mathbf{a}_2^*$) can be determined from the equation:

$$\mathbf{a}_j^* = \frac{2\pi}{a_i \sin\gamma} \quad \text{and}$$

$$\mathbf{a}_i^* \perp \mathbf{a}_j \qquad \text{for } i \neq j$$

Here $\gamma$ is the angle between $\mathbf{a}_1$ and $\mathbf{a}_2$. The utility of reciprocal space analyses in LEED is that the diffraction pattern is a direct representation of the reciprocal lattice, as shown next.

Low Energy Electron Diffraction (LEED)

Having established the classification of periodic surface structures, we can elucidate the physical origin of electron diffraction phenomena. The discovery of interference phenomena in processes where electrons are scattered by crystals played an important role in the development of quantum mechanics. L. de Broglie[28] postulated that an electron (or any particle) with velocity $v$ and mass $m$ exhibits a wave nature with wavelength $\lambda=h/mv$, $h$ being Plank's constant. Thus, the wavelength for 100 eV-electrons is about 1.2 Å, a value which leads to interference in periodic crystal lattices. The technique of LEED uses an electron gun to generate a collimated beam of electrons which is then aimed at a crystal surface. The electrons scatter off the surface according to processes that depend on the geometry of the surface, as well as its elemental composition.

The surface sensitivity of LEED results from two effects. First, in the LEED energy range the mean-free-path for inelastic scattering of the electron is very short,

typically only about 5 Å. The properties of this parameter are discussed more extensively in the following chapter, but we note that LEED operates in the energy range in which the mean-free-path is typically at its smallest value, so that electrons penetrating more than two or three atomic layers into the solid have a high probability of losing energy (and coherence) relative to the incident beam and thus being lost from the elastically diffracted flux. A second source of surface sensitivity in LEED is the elastic scattering itself; backscattering is very strong (ion core cross-sections may be as large as 1 $Å^2$) so that successive atom layers receive smaller incident electron fluxes and contribute less to the scattering. Typically, these two effects contribute equally to the surface sensitivity.

The formation of a diffraction pattern is illustrated schematically in Fig. 3. Here $\mathbf{a}_1$ and $\mathbf{a}_2$ are the unit vectors in real space. The wave vector $\mathbf{k}_0$ characterizes the incident wave, and the directions of interference maxima are determined by a set of wave vectors $\mathbf{k}$. $\mathbf{k}_0$ and $\mathbf{k}$ must satisfy the well-known Bragg law:

$$\mathbf{k} - \mathbf{k}_0 = \mathbf{q} = h\,\mathbf{a}_1^* + k\,\mathbf{a}_2^* \qquad (2.3)$$

where $\mathbf{q}$ is any reciprocal lattice vector, $\mathbf{a}_1^*$ and $\mathbf{a}_2^*$ are the reciprocal unit vectors, and h and k are integers. The Bragg law is equivalent to the Laue condition,[29] which determines the allowed diffraction events consistent with translational invariance in two dimensions. This can be seen by multiplying Equation (2.3) by $\mathbf{a}_1$ and $\mathbf{a}_2$:

$$\mathbf{a}_1\cdot(\mathbf{k} - \mathbf{k}_0) = h\,\mathbf{a}_1\cdot\mathbf{a}_1^* + k\,\mathbf{a}_1\cdot\mathbf{a}_2^* = h$$

$$\mathbf{a}_2\cdot(\mathbf{k} - \mathbf{k}_0) = h\,\mathbf{a}_2\cdot\mathbf{a}_1^* + k\,\mathbf{a}_2\cdot\mathbf{a}_2^* = k \qquad (2.4)$$

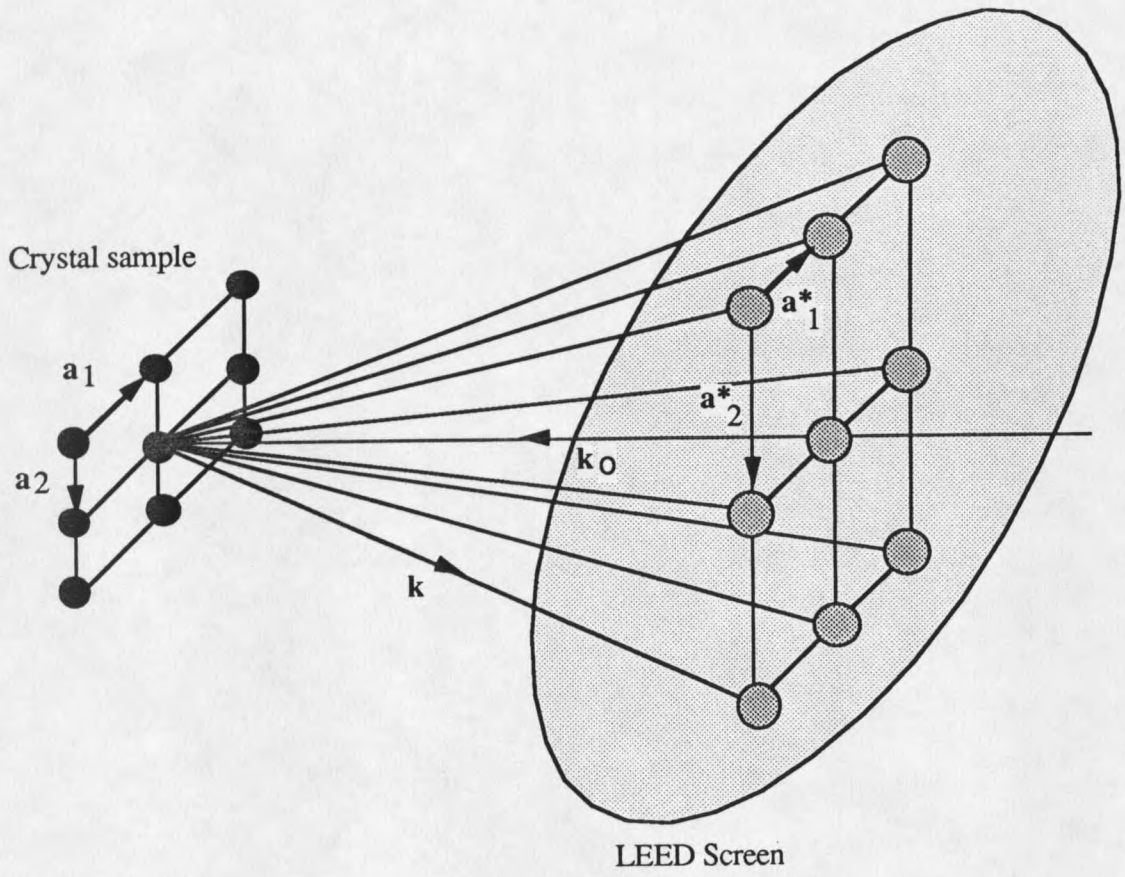


Fig. 3: The principle of the formation of a diffraction pattern in LEED experiment.

The vectors **k** specify the directions of interference maxima; these are given by the points where the diffracted beams intersect the fluorescent screen, displaying the "diffraction spots" in LEED experiments. From the Equations (2.3) and (2.4), one can see that the LEED pattern is an image of the surface reciprocal lattice when viewed along the surface normal at a great distance from the crystal. To determine the directions of the scattered beams, one uses the Ewald construction. Since for a purely planar lattice mesh the periodic repeat distance is effectively infinite in the z direction, the reciprocal lattice "points" along the surface normal are infinitely dense - one speaks of a rod in reciprocal space. The Ewald sphere is constructed with a radius of $2\pi/\lambda$ and is centered at a point

$|\mathbf{k}_0| = 2\pi/\lambda$ length units from the origin of the reciprocal lattice in the direction of $\mathbf{k}_0$, and points to the origin of the reciprocal lattice. The intersections of the reciprocal lattice rods with the sphere satisfy the Laue condition and therefore determine the directions of the diffracted beams .

The existence of a sharp spot pattern implies the existence of a well-ordered surface. In principle, the diffraction spot pattern (i.e., the location of the diffraction spots) only provides information on the periodicity of the surface. However, one can often infer additional information about the following surface attributes from the LEED pattern:

(1) Surface crystallography. In the presence of adsorbate layers or in clean surface reconstructions, the LEED pattern may have a periodicity different from the unreconstructed clean surface, especially when a superlattice is present. For example, a $(\sqrt{3}\times\sqrt{3})$ adsorbate superlattice on a Si(111) surface has a unit mesh area three times larger than the area of the substrate unit mesh. We can guess that the atomic geometry may involve a one-third monolayer adsorbate coverage, each atom occupying a symmetrically identical site. An important point is that neither the number nor the positions of atoms within the unit mesh affect the positions of the diffraction spots. Therefore, several different adsorbate coverages and site locations may be consistent with a given spot pattern.

(2) Domain structures. The symmetry information from a LEED pattern reflects the symmetry properties of the surface itself. The surface atomic arrangement can have at most the symmetry indicated by the LEED pattern; the true surface structure could possess a lower symmetry. This latter situation occurs, for instance, when the surface contains domains, in which different patches of the surface coexist to form the long-range imperfection. These different patches have mutually identical structures, but they do not mesh together without breaks in the periodicity. If the mean diameter of the domain is

greater than the transfer width, which is typically in the range of 5~10 nm and controlled by experimental considerations,[25] the LEED pattern consists of a superposition of intensities associated with interference caused by the separate domains.

(3) Steps, Kinks, and Defects. Additional information can be obtained by probing the variation in diffracted intensity across the width of a single spot, the so-called spot profile. If the surface contains steps, kinks, and other defects, the LEED pattern will exhibit features due to the superposition of the amplitudes of the electron waves scattered in the different regions, leading to spot broadening or spot splitting, formation of streaks, etc. These effects can be understood using the reciprocal lattice rod construction. Any deviation from perfect two-dimensional periodicity will destroy the ideal delta-function character of the rods,[30] for instance, the reciprocal lattice rods for a regular stepped surface contain two sets of rods as illustrated in Fig. 4, leading to the existence of extra spots. Some possible surface defect structures, the corresponding modification of the reciprocal lattice rods and the resultant LEED spot profile are also shown in Fig. 4.

(4) Degree of Structural Disorder. Electron-diffraction spot profiles can be used to elucidate the degree and character of the surface long-range order. The angular spread of the intensity maxima is inversely proportional to the mean diameter of the periodic structures as can be derived from Equation (2.4)

(5) Growth information. Often the LEED intensity distribution around the diffraction spots is a strong function of the incident-electron kinetic energy. This is called the size effect and indicates two-dimensional island formation.[31,32]

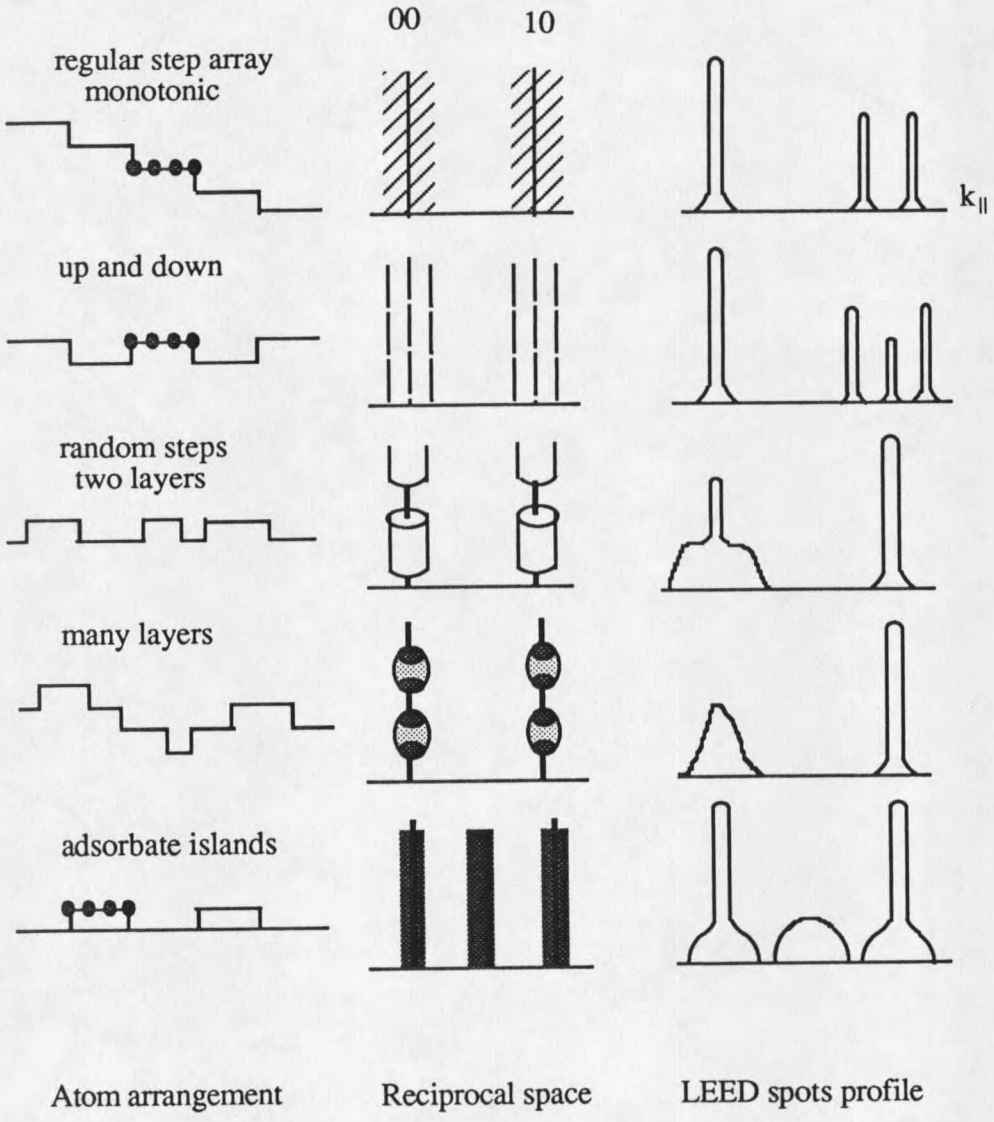


Fig. 4: Some examples of surface defects, the corresponding modification of the reciprocal lattice rods and the resultant LEED spot profile.

Up to this point in the discussion only the positions of the LEED spots have been considered. To determine surface structural information beyond that discussed above, we must attempt to interpret not only the diffraction pattern, but the diffracted beam intensities as functions of incident electron energy, the so-called I-V curves. The procedure used to determine the geometrical arrangement of surface atoms from LEED intensities is as follows. First, a model of the atomic arrangement is postulated that is consistent with the symmetry of the LEED pattern. Then, the I-V curves are calculated using LEED theory in the first few atomic layers, based on the postulated geometry. Finally, the resulting I-V curves are compared to experiment and the process is repeated with a refined geometry until satisfactory agreement is obtained. It must be emphasized that this is a highly non-trivial procedure that involves significant computing effort and that the process does not lead to a unique solution in every case. We will discuss this issue in detail in the next chapter.

Auger Electron Spectroscopy

Auger electron spectroscopy (AES) was used to characterize the elemental composition of the sample surface. In this section, the essential ingredients of this technique are described.

A high-energy beam of electrons with kinetic energies in the range of 1 to 10 keV is applied to bombard the sample surface. The electron incident on the sample creates a hole in one or more of the substrate atomic core levels. The ionized atom subsequently decays by one of two mechanisms. One is the Auger process. Referring to Fig. 5, the hole initially created in the K shell, for example, is filled by an electron from the L shell, for example, simultaneously ejecting a second electron from the L shell. This ejected electron is called the Auger electron and has a kinetic energy approximately equal to $E_K$-$2E_L$, where $E_K$ and $E_L$ are the binding energies of the K and L shells, respectively. That is, the energy gained by the ion when the outer shell electron makes a downward transition to fill the

inner shell hole is carried away as kinetic energy by the Auger electron. Since the energy-level diagram is different for each element, the Auger electron has a kinetic energy that is unique to a specific atomic transition and thus is sensitive to elemental types. However, as can be seen from Fig. 5, there are many possible final states of the same energy, one corresponding to each of the two-hole final-state wave functions of the L-shell. The same description can be applied to other pairs of shells and final states involving these shells, leading to a characteristic complicated secondary electron emission spectrum.

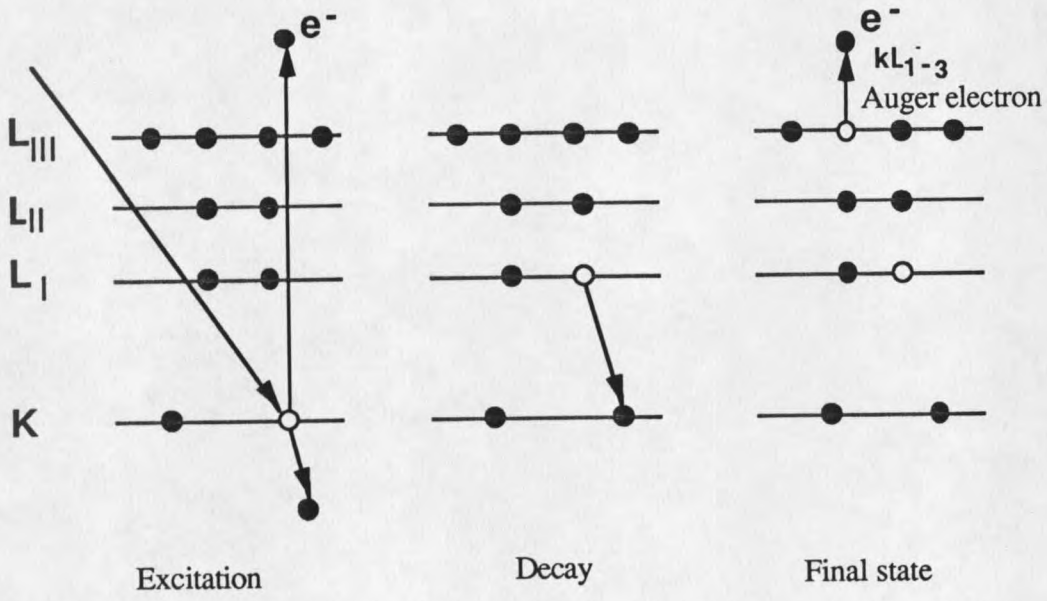


Fig.5: Schematic of Auger process.

A relaxation mechanism that competes with Auger emission is radiative de-excitation, in which the relaxation energy is carried away by a characteristic x ray. However, the cross-section of x-ray emission in the core-level binding-energy range of interest to us is usually negligible compared with that of AES. The ratio of the probability

of x-ray emission, $P_X$, to the probability of Auger electron emission $P_A$ is given empirically[33] as a function of atomic number Z by $P_X/P_A = (-6.4\times10^{-2}+3.40\times10^{-2}Z - 1.03\times10^{-6}Z^3)$. The probability of Auger emission is greater than that of the x-ray emission for atomic numbers lower than arsenic, $Z \doteq 33$.

Because of the large incident-beam flux and the multitude of open relaxation channels in a solid, the characteristic Auger electrons appear as small peaks on top of a slowly varying secondary-electron energy distribution N(E). Hence, in practice one usually measures the derivative of the energy distribution function to suppress this large background. In general, the peaks used to identify the elemental composition of the sample occur in the energy range of 50~2400 eV; elements are identified by comparing the measured spectra with published "standard" spectra.[34]

Auger analysis is sensitive to the elemental composition of only the first few atomic layers. The surface sensitivity of this technique is due to the small escape depth of electrons in the 50~2400 eV kinetic energy range,[35] typically about 5~30 Angstroms. Hence, in Auger electron spectroscopy the volume of the analyzed region near the surface is proportional to the escape depth and the electron beam spot area.

The essential components of an Auger electron spectrometer are a primary beam source ( usually electron gun), the sample, and an analyzer and detector system. In our system, a retarding field grid system was used in combination with the LEED technique, as described in the next section.

## Experimental Apparatus

In this section, we shall briefly examine the most important components of the reverse view-LEED-Auger system; the electron gun, the electron analyzer, electronics and computer interface. Fig. 6 is a schematic diagram of the basic units of this system.

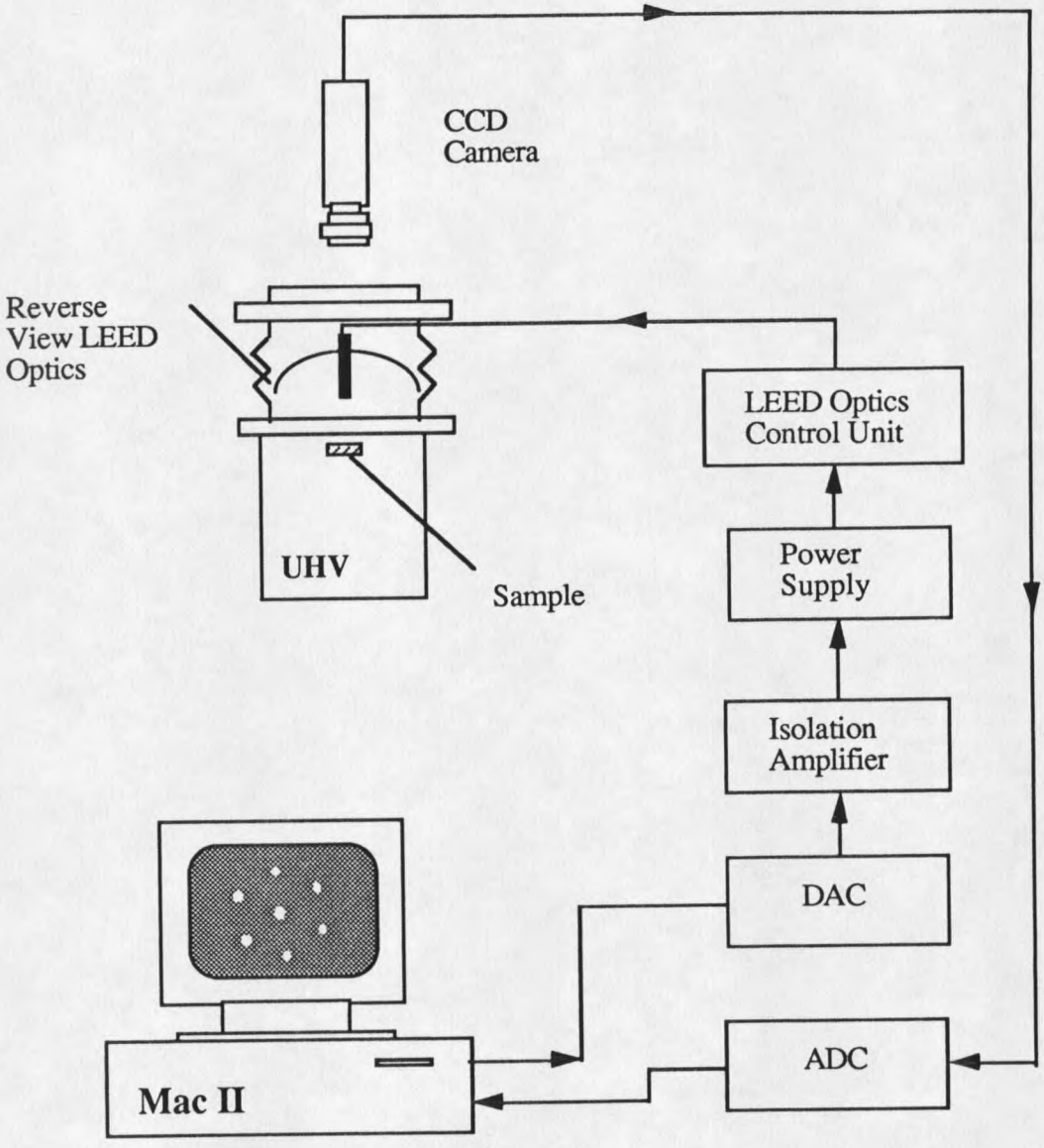


Fig.6: Schematic diagram of the LEED experimental system.

Experimental Layout

Our LEED/Auger optics system is a Princeton Research Instruments Reverse view LEED unit (model RVL 10-120), which consists of a source of primary electrons and a 4-grid hemispherical retarding field electron energy analyzer. An electron gun provides a beam that is incident normal to the sample surface; the gun is also capable of operation at low energies. The electron beam diameter is less than one millimeter. For LEED measurements the system operates down to primary energies of less that 10 eV. The use of the electron gun in conjunction with the hemispherical-grid energy analyzer allows the same electron optics to be used for both LEED surface structural analysis and Auger spectroscopy surface chemical analysis. In its basic configuration, a retarding-field analyzer has four nested hemispherical grids and a hemispherical glass collector screen coated with a transparent oxide coating and a layer of fluorescence material.

LEED Mode

In the LEED mode, the sample, and the first and fourth grids are at ground potential and a field-free region is created between the sample and the first grid. An electron-retarding voltage equal to the value of incident electron energy is applied between ground and both the second and third grids (the use of two grids here instead of one enhances the energy resolution.[25]) to create a high-pass filter, since only elastically scattered electrons will have enough energy to pass through these grids. A further retarding voltage is applied between the hemispherical collector and the outermost (fourth) grid to suppress stray low-energy electrons. Since the collector is at a positive voltage relative to ground (typically 4~5 keV), the elastically scattered electrons that pass though the fourth grid will accelerate and hit the phosphor screen with enough energy to cause the screen to glow.

Auger Mode

In the Auger mode, the energy distributions of Auger electron emitted from the sample were measured by the retarding field technique.[36] As shown in Fig. 7, a negative ramping voltage $U_r$ is applied between $G_{23}$ and $G_1$ (grounded), so that all electrons with kinetic energies less than $U_r$ are repelled and do not arrive at the collector. The collector is biased 240 eV (positive) to aid collection of slow electrons emerging from the grid section and to inhibit secondary electron emission from the collector itself. In order to improve the resolution, sample modulation instead of grid modulation was selected with a voltage of ~6 V peak to peak by coupling to the sample through a transformer.[36] The Auger current is measured by a lock-in amplifier through a 1 MΩ resister. During the measurement the beam current and the voltage were kept at about 10 μA and 2 keV, respectively. Using this set-up, we obtained a typical resolution of 6 eV, adequate for adlayer coverage studies and contamination checks.

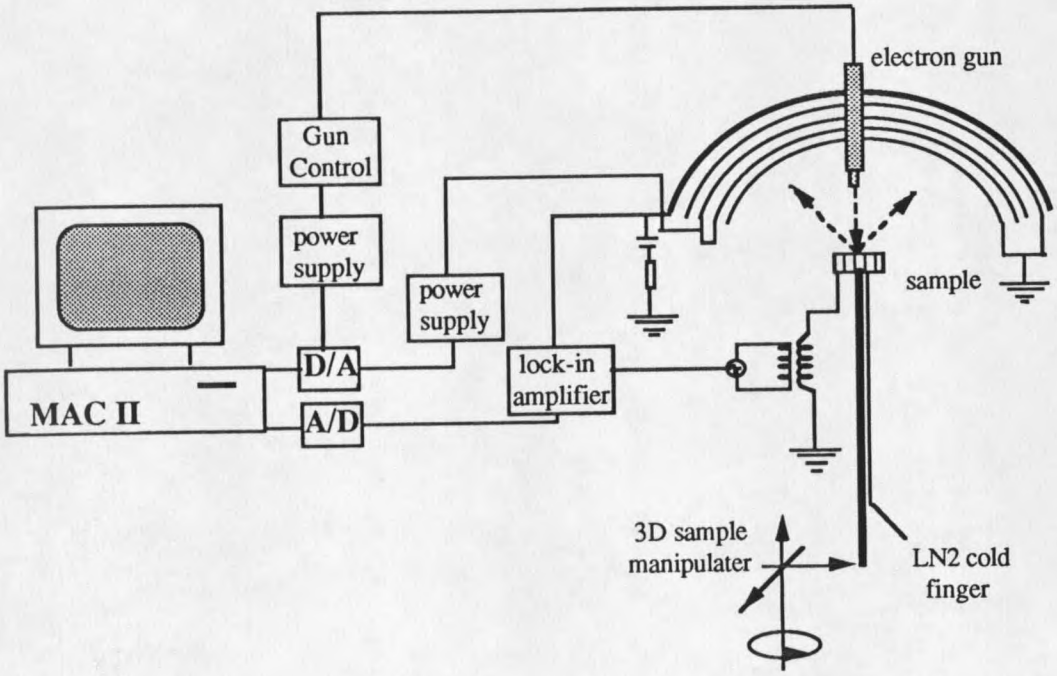


Fig. 7: Circuit for using LEED system as a retarding field analyzer.

Data Acquisition

The computer system controls the electron gun energy for the LEED measurement and drives the ramping voltage; it also measures and plots the Auger signal for Auger measurements.[37] A variable voltage is provided for both purposes by a Kepco operational power supply over a range of 0~700 V with an accuracy better than 0.2 V. This voltage is fed into the Physical Electronics LEED control unit.

LEED images are captured by a high-resolution CCD camera manufactured by Pulnix ( model TM-840), which has a 2/3-inch, high-resolution CCD solid-state imager with 800×490 pixels. In its integrating mode the camera can inhibit the read-out of the optical signal for an integral number of complete video frames. During this time, the CCD continues to accumulate an optical signal until it is read out by the video circuitry. This is extremely useful for low-light situations as in LEED imaging. The video output is a 1 V p-p signal with a 50-dB signal-to-noise ratio that provides one frame every 1/30 s. The camera output can be directly fed into the computer hardware.

An Apple Macintosh II microcomputer is used to control the experiment and for data acquisition. The computer has 5 Mbytes of RAM, a 15.6672-MHz MC68020 processor with a MC68881 numerical coprocessor, a color monitor, and 40 Mbytes of hard disk storage. An Apple Tape Backup 40SC is used for additional storage. Two interface cards are used, a MacADIOS II which provides an analog-conversion resolution of 12 bits for the high-voltage ramp, and a Data Translation Quick-Capture frame grabber, which consists of an 8-bit video A/D converter with 12.5 MHz conversion rate. Every picture (or frame) uses 512 kbyte of memory and can be stored and accessed at any time inside the computer.

Software

Both the data-acquisition and data-analysis software were developed in our group. The program, called MacLEED, is written in C and utilizes the standard Macintosh User Interface Toolbox routines.[38] Three types of data acquisition can be achieved using this package: First, the real-time picture can be displayed on the computer monitor, for assistance in adjusting experimental parameters, and snapshots of the diffraction pattern can be taken and the diffraction spot intensity evaluated on-screen; Second, complete screen images can be accumulated by summing the video signal over a specified number of frames, and the spot profile of selected regions along arbitrary directions can be plotted on the screen. Third, the diffraction beam intensities can be measured as a function of the incident electron beam energy to form what are called I-V curves; this is the most important application for our studies since the atomic structure may be determined through I-V curve analysis using multiple scattering theory.

## Sample Preparation

In our studies, silicon and germanium single crystals were used as samples. The orientation of both surfaces was along [111] directions. We used wafers for silicon and a cleaved crystal bar for germanium.

Sample Cleaning

Our Si(111) wafers were p-type (boron doped) with a resistivity of ~ 20 Ω-cm. The wafer was cut to a 1/2"×1/8" rectangle and mounted in two brass blocks which receive ohmic heating contacts made of two 0.1-mm Ta clips, as shown in Fig. 8. The sample was heated directly by passing current through it. The heating current was approximately 4~8 A; this heats the sample to temperatures as high as 1100 °C. The sample

was cleaned outside the chamber by the process described in Ref. 39. A pure annealing treatment was used inside the chamber. The recipe for the annealing process is as follows:

(i) Outgas the sample holder and sample below 600 °C at which temperature the oxide layer is removed, until the pressure stays below $1\times10^{-9}$ torr. This may take several hours.

(ii) Raise the temperature rapidly to 1150 °C and hold it constant for 1 to 2 min annealing time. The pressure should stay at $10^{-9}$ torr or below.

(iii) Cool slowly at rates of < 2°/sec from 900 °C to room temperature. This is to avoid the occurrence of diffuse scattering due to rapid cooling.[39] Auger analysis usually showed no surface impurities other than some residual carbon, sometimes present at a small fraction of one monolayer.

Once a sample is cleaned in this manner, it can be cleaned repeatedly. Adsorbed Bi or Sb can be removed by flashing to 1150 °C.

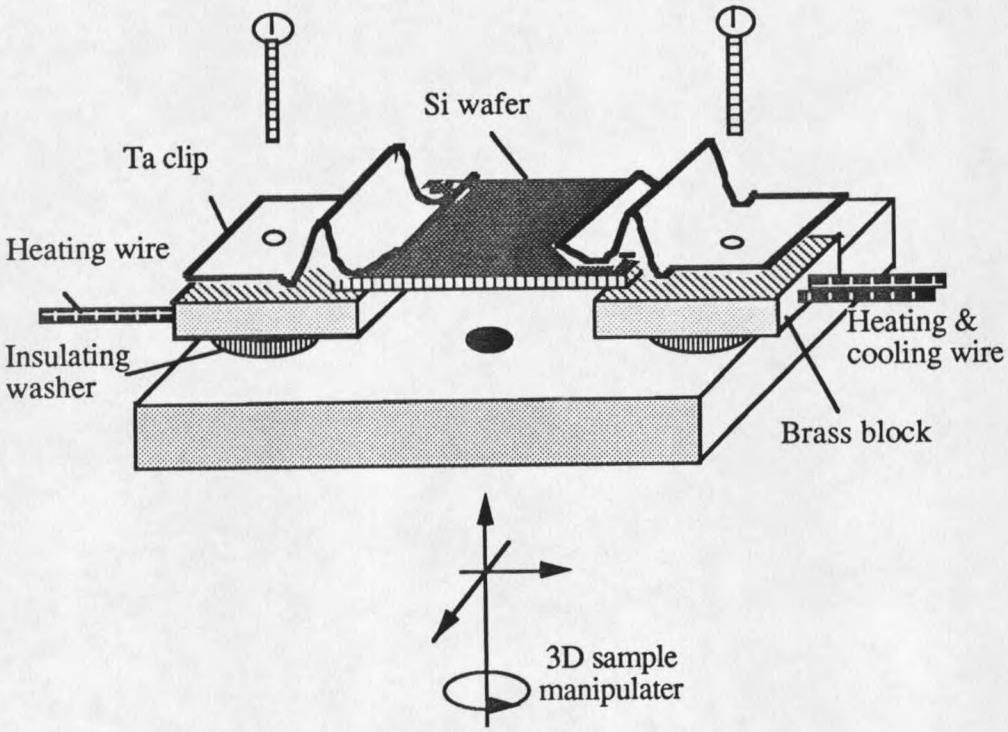


Fig. 8: The sample holder for Si wafer sample.

The n-type Ge single crystals with a 40 Ω-cm resistivity were cut into 5 mm square bars oriented to within 0.5° along the [111] direction. Using a diamond saw, notches 0.051" deep and 0.020" wide were cut into the side of each bar at 0.085" intervals to assist in the cleaving process under UHV; the sample holder is illustrated in Fig. 9. The depth of the notches must be carefully controlled so as to match the pitch of the cleaving blade to get a good cleave.

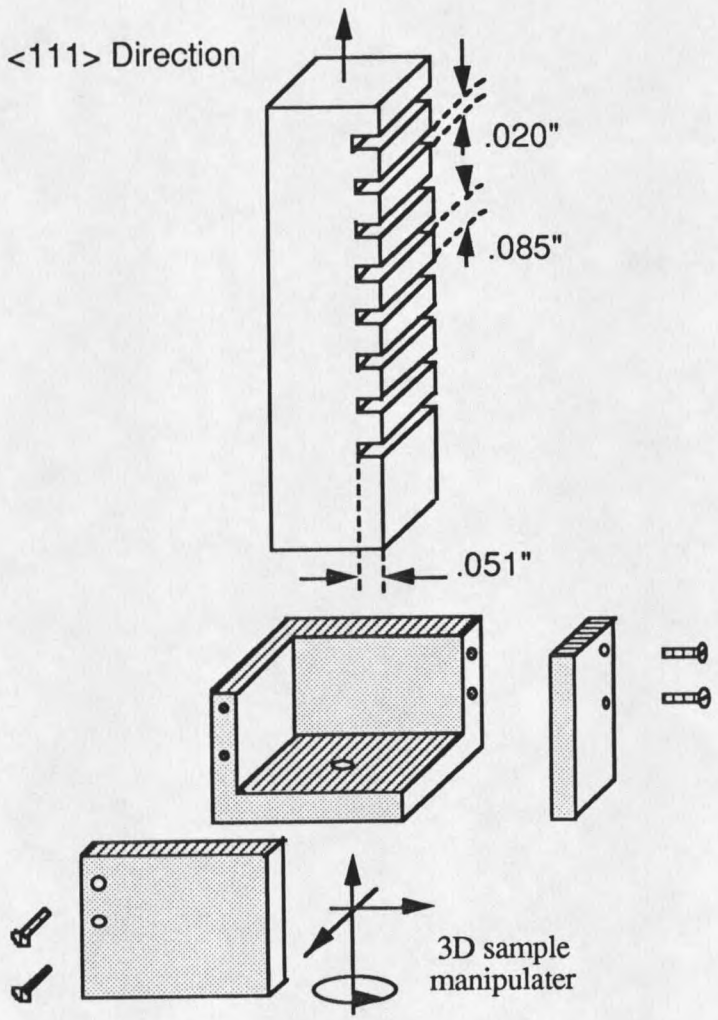


Fig. 9: The Ge sample for cleaving and the sample holder.

Thin Films Deposition

The Bi and Sb films were deposited onto the clean substrate by sublimation from high-purity (6N) polycrystalline material held in a shielded tungsten wire basket heated to the sublimation temperatures of bismuth and antimony, typically ~600 °C for Bi and ~450 °C for Sb, by passing current through the baskets. A slow deposition rate (typically 1 Å/min) was used and was monitored with a quartz-crystal oscillator (QCO), which was mounted directly beside the sample and calibrated by Rutherford backscattering in a separate chamber. Before deposition, the evaporator was well outgassed so that the pressure was below $5\times10^{-10}$ torr during deposition.

## QCO Calibration

The change in frequency of the quartz crystal was calibrated to the bismuth coverage on the sample in the following manner: a quartz crystal has several vibrating modes, corresponding to certain resonant frequencies. The operating mode used in so-called micro-balance applications is the shear mode along the AT-plane.[40] The resonant frequency of the quartz crystal used in our studies was typically 5 MHz, and the frequency change for a few monolayers coverage was normally in the range 10~100 Hz. Over such a small frequency interval, the relationship between the frequency change $\Delta f$ and the mass of the adsorbed material $\Delta m$ is nearly linear, and can be expressed as

$$\Delta f = C\,\Delta m \tag{2.5}$$

with C a constant dependent on the specific quartz crystal. Since

$$\Delta m = \rho A \Delta \tau \tag{2.6}$$

where ρ is the mass density of the adsorbed material, A is the area of the deposition which is a constant, and $\Delta\tau$ is the thickness, equation(2.5) can be written as

$$\Delta f = (\frac{1}{k})\,\rho\Delta\tau \qquad (2.7)$$

with $k = \frac{1}{CK}$, which is referred as the instrument sensitivity, and was determined to be $3.009\times10^{-8}$ in cgs units in our system. $\rho\Delta\tau$ gives the surface mass density of adsorbed material.

From the above formula, it is easy to obtain the relationship between the coverage and the change of the quartz crystal frequency if we assume that the sticking coefficient for either Bi or Sb on the quartz crystal is equal to that for the substrate. In the equation above, the product $\rho\Delta\tau$ is the surface mass density, with units ($g/cm^2$), of the overlayer material. For Si and Ge(111) surfaces, the atomic densities are $7.89\times10^{14}$, and $7.22\times10^{14}$ atoms/$cm^2$, respectively. The surface mass density was found by multiplying the atomic density by the ratio of the mass number of Bi or Sb divided by Avogadro's constant. The frequency changes for one monolayer of Bi and Sb on the Si(111) and Ge(111) surfaces computed from the above equation are summarized in Table 1

TABLE 1: QCO frequencies for 1 ML adsorbates on Si(111) and Ge(111) substrates.

| substrate / adsorbate | Si(111) (Hz) | Ge(111) (Hz) |
|---|---|---|
| Bi | 9.10 | 5.30 |
| Sb | 8.32 | 4.85 |

# CHAPTER 3

# MULTIPLE SCATTERING THEORY

## Introduction

Since low-energy electrons scattered from crystal surfaces penetrate only a few atomic layers, they carry useful information about the surface structure. To determine adsorbate-substrate atom registry and to obtain detailed structural information, it is necessary to analyze the beam intensities as functions of the incident electron energy, the I-V curves. In order to make the link between beam intensities and atomic positions, we must understand both the basic electron scattering mechanism at LEED energies. Analysis of the I-V curve relies on comparison between the measured intensities of scattered electrons and intensities predicted by calculations for model surfaces. These model surfaces can be progressively refined to fit the observed data as closely as possible. Here, the term "theory" includes the basic understanding of both the electron scattering mechanism and the nature of electron diffraction at LEED energies. Two types of LEED theory, kinematic and dynamical theories, have been established over several decades.

## Kinematic Theory to Dynamical Theory

The kinematic theory is based on the assumption that all atoms scatter electrons independently and participate only once in the scattering process. This description leads to

a relatively simple theory and has been quite successful in the interpretation of diffraction in x-ray diffraction and high energy electron diffraction.[24] However, the single scattering assumption does not hold at low primary energies, and rather elaborate calculations are required to predict the intensities; in other words, a dynamical theory has to be applied.

Even though there have been several different formulations to describe the LEED process, most include the same basic physical processes and produce very similar predictions. The essential ingredients of dynamical theory must provide adequate descriptions of the following processes:

(a) Crystal potential scattering. Because electron ion-core scattering cross sections are large, a description of the multiple scattering between the incident electron and the ion cores of the solid is an essential ingredient of any theory of LEED. An additional contribution to the interaction potential is derived from the exchange potential among the diffracting electrons. We use crystal potential to express all the contributions above. The potential energy for the scattering incorporates various forces acting between the diffracting electron and the surface: The Coulomb force that attracts the electrons toward the nuclei; the screening of the nuclei by core electrons; and the Pauli exclusion force among the diffracting electrons, through which electrons tend to avoid each other.

(b) Inelastic scattering. The interaction of the incident electron with the valence electrons in the solid causes inelastic attenuation of the elastic wave field within 5-10Å of the surface. The microscopic origin of most of this damping is thought to be large-energy ($\Delta E>2eV$) electron-loss processes associated with interband and intraband transitions and plasmon excitation in the solid.[41] This effect produces the short mean free path for electrons in matter, and is in turn the basis for the high surface sensitivity of LEED. Consequently the

effects of both multiple scattering and inelastic collisions must be described in an adequate theory of LEED.

(c) Temperature effects. Another damping effect that must be incorporated in a description of electron scattering is that due to the low-energy ($\Delta E \sim 10$ meV) collective atomic vibrations (phonons), which reduce the intensities of the diffracted beams and increase the background intensity.

(d) Multiple scattering. The multiple scattering of an electron from the crystal may be regarded as made up of a sum over paths of an electron undergoing sequential individual scattering events.

## The Intensity Calculation in Dynamical Theory

We now consider the calculation of diffraction intensities for a plane wave representing the incident electron beam; we assume a periodic and defect-free crystal surface as our target. The approach is a generalization of the work of Beeby, following the ideas of the Korringa-Kohn-Rostoker (KKR) approach.[42~44] The scattering process is treated in a hierarchy of steps. In principle, the potential responsible for scattering of the LEED electrons should be considered non-local and should contain exchange and correlation effects in a self-consistent manner. However, a rather simple local potential, a "muffin-tin" potential, is used as approximate evaluation and provides surprisingly good results.[44] In this potential, within spheres around the individual ion cores a spherically symmetry is used, while in the region left the potential is taken to be constant. The advantage of the muffin-tin potential is that the scattering by single atoms can be described by just a set of phase shifts, and the electron propagation between atoms can be simply

described by free-space wavefunctions. The net scattering process then can be simplified by considering scattering from individual atoms plus the multiple scattering among the point scatterers. The semi-infinite crystal surface is replaced by a slab of several layers parallel to the surface. A layer may consist of several subplanes; each layer or subplane exhibits translational symmetry. The solution of the general problem is achieved by constructing, in turn, the electron-diffraction characteristics of a single atom, a subplane, individual layers of atoms and, finally, stacks of such layers comprising the model slab, as schematically illustrated in Fig. 10.

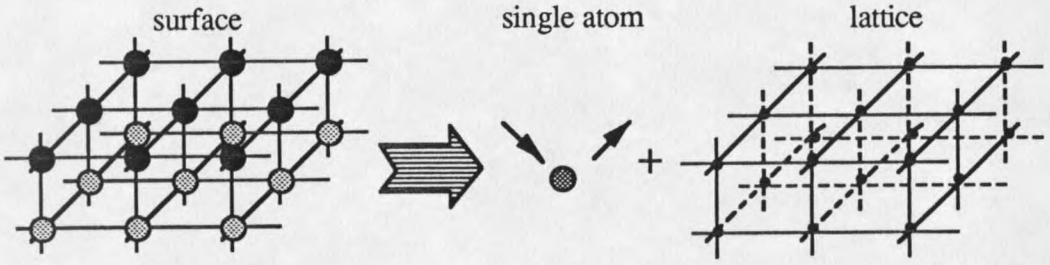


Fig.10: Schematic description of the individual atom and point scattering.

Ion-core Scattering

The first step in the scattering process, ion-core-scattering, is treated by assuming spherically symmetrical interaction potentials surrounded by regions of constant potential (the muffin-tin model). The constant potential, or inner potential, consists of both a real ($V_{or}$) and an imaginary ($V_{oi}$) part. The real part is related to an effective index of refraction of the crystal that describes the change in the electron's kinetic energy inside the crystal relative to its energy in the vacuum. The primary effect of variations in $V_{or}$ is to shift the peaks in the I-V data along the energy axis. The imaginary part $V_{oi}$ serves solely to characterize the electron's energy loss through inelastic collisions, and accounts for the attenuation and mean free path, discussed in detail below. In quantum mechanics, the

scattering of a plane wave of wave vector $\mathbf{k}_o$ by a spherically symmetric potential is completely defined by the partial-wave phase shifts, since the electron moves in free space between the individual potentials. The Hartree-Fock equation describing electron-solid scattering is[45]

$$[\frac{-h^2}{2m}\nabla^2 + V_{all}(\mathbf{r}) - E]\cdot\phi_o(\mathbf{r}) = 0 \tag{3.1}$$

where $V_{all}$ is the muffin-tin potential. Since the potential is assumed to be spherically symmetric, the scattered wave has the following asymptotic form:

$$e^{i\mathbf{k}_0\cdot\mathbf{r}} + t(\theta)\cdot\frac{e^{i\mathbf{k}_0\cdot\mathbf{r}}}{r} \tag{3.2}$$

where $\theta$ is the scattering angle and $\mathbf{r}$ is the displacement vector relative to the atomic center. The scattering amplitude $t$ ($\theta$) (called the t-matrix) is expanded into partial waves in the form of Legendre polynomials, *viz.*[46]

$$t(\theta) = 2\pi \sum_{l=0}^{\infty}(2l+1)t_l\ P_l\ (\cos\theta) \tag{3.3}$$

where $t_l$ is given by

$$t_l = \frac{\exp(2i\ \delta_l) - 1}{\mathbf{k}_o} \tag{3.4}$$

Phase Shifts

All the crystal potential information is not expressed explicitly in Equation (3.3) and

can be included in the calculation of the phase shifts. In order to compute the phase shift, the muffin-tin potential $V_{all}$ in Equation (3.1) must be specified. In the overlapping-charge-density model developed for the study of semiconductors,[45,47] $V_{all}$ can be characterized as a sum of the crystal potential and the exchange potential:

$$V_{all} = V_\alpha + V_{ex} \tag{3.5}$$

For a particular ion core labelled by $\alpha$, $V_\alpha$ is expressed in terms of the electronic charge density $\rho_\alpha(r)$, the atomic number $Z_\alpha$, and the ionicity $I_\alpha$, as

$$V_\alpha(\mathbf{r}) = \frac{-Z_\alpha e^2}{|\mathbf{r}|} + e^2 \int d^3r' \frac{\rho_\alpha(\mathbf{r}')}{|\mathbf{r}-\mathbf{r}'|} + \frac{I_\alpha M e^2}{d} \tag{3.6}$$

where the first term is the Coulomb interaction between the electron and the nucleus. The second term represents the electrostatic force between the diffracting electron and all the point charges present inside the muffin-tin potential; the integration can be simplified by assuming that the charge density $\rho_\alpha$ is spherically symmetric, e.g. $\rho_\alpha(\mathbf{r}) = \sigma_\alpha(r)/4\pi r^2$. The last term contains the electrostatic Madelung sum **M** for the crystal lattice,[48] and d is the nearest neighbor distance. Note that the charge density is constructed from the occupied electronic wave functions; thus the Hartree-Fock equation must be solved self-consistently.

An additional contribution to the interaction potential is related to the Pauli exclusion principle, according to which electrons of the same spin repel each other. This effect is treated by the exchange potential. In most LEED calculations, the Slater model[49] or the Hara model[50] are used to represent the exchange effect.

Once the muffin-tin potential has been specified, the phase shifts can be calculated through the radial Schrödinger equation

$$\left(\frac{\hbar^2}{2m}\right)\frac{d^2R_l\ (r)}{dr^2}+\left[V_\alpha(r)+V_{ex}\{\rho(r)\}+\frac{l\ (l\ +1)\hbar^2}{2m\hbar^2}\right]R_l\ (r)=(E+V_0)R_l\ (r) \quad (3.7)$$

The equation is solved numerically inside the muffin-tin spheres. The phase shifts can be obtained from the boundary condition that the solution of the radial equation inside the muffin-tin sphere match smoothly to the solution outside. The logrithmic derivative of the wave function $R_l(r)$ is matched to the solution outside the muffin-tin potential, which consists of spherical Bessel functions $j_l$ and $h_l$

$$\frac{R'_l\ (r_m)}{R_l\ (r_m)}=\frac{\exp(i2\delta_l\ )h_l^{(1)'}(kr_m)+h_l^{(2)'}(kr_m)}{\exp(i2\delta_l\ )h_l^{(1)}(kr_m)+h_l^{(2)}(kr_m)} \quad (3.8)$$

This yields

$$\exp(i2\delta_l\ )=\frac{L_l\ h_l^{(2)}(kr_m)-h_l^{(2)'}(kr_m)}{h_l^{(1)'}(kr_m)-L_l\ h_l^{(1)}(kr_m)},\quad \text{with}\quad L_l=\frac{R'_l\ (r_m)}{R_l\ (r_m)} \quad (3.9)$$

Inelastic Effects

We now discuss how inelastic scattering processes are customarily treated in LEED theory. The inelastically scattered electron is treated in terms of a decrease of elastic-beam intensities. This is achieved by introducing a mean free path, or alternatively, an imaginary part of the electron-surface interaction potential. Furthermore, quasi-elastic interactions with collective excitations can give rise to momentum transfers that move electrons into the

diffuse background between spots, where they play no role in the I-V analysis. The justification for representing all the inelastic processes by a single quantity is that in elastic LEED we need only know what fraction of the LEED electrons lose energy. In general, the electronic mean free path is energy dependent, since the inelastic processes are energy dependent. However, the mean free path is relatively independent of the material, so that one may speak of a "universal curve" of mean free path vs. electron energy. According to this curve, LEED electrons probe a surface region that extends to no more than 10~20 Å in depth for the usual energies (20~300 eV). The mean-free-paths shown in Fig. 11 correspond to an imaginary part of the potential of approximately 1 to 5 eV. The actual method of including inelastic scattering in LEED calculations is rather simplistic. The damping of an electron wave is included by making the potential inside the crystal complex, viz. $V_{or}+iV_{oi}$. Here, $V_{or}$ and $V_{oi}$ are the real part and the imaginary part of the inner potential. Therefore the wave vector $\mathbf{k}$ and the kinetic energy E of electron in the vacuum are related by $k^2/2=E$ (we use $\hbar^2/m=1$, atomic units). After the wave has penetrated the surface, we can ignore the scattering by the atomic cores, write this wave in the form $\exp(i\mathbf{k}'\cdot\mathbf{r})$, where $\mathbf{k}'$ is the wave vector below the surface, with $k'^2/2=E+V_o=E+V_{or}+iV_{oi}$. $V_{oi}$ is used to represent all inelastic effects. Thus, the wave vector $\mathbf{k}'$ must be complex, and accordingly we may write

$$\frac{1}{2}k'^2=\frac{1}{2}(k'_r+k'_i)^2=\frac{1}{2}(k'^2_r-k'^2_i)+ik'_r k'_i=E+V_{or}+iV_{oi} \qquad (3.10)$$

Where $k'_r$ and $k'_i$ are the real and imaginary parts of the wave vector $\mathbf{k}'$. The real part and imaginary part of the wave vector can be calculated by equating real and imaginary parts of (3.10)

$$\frac{1}{2}(k'_r{}^2 - k'_i{}^2) = E + V_{or} \tag{3.11}$$

$$k'_r\, k'_i = V_{oi} \tag{3.12}$$

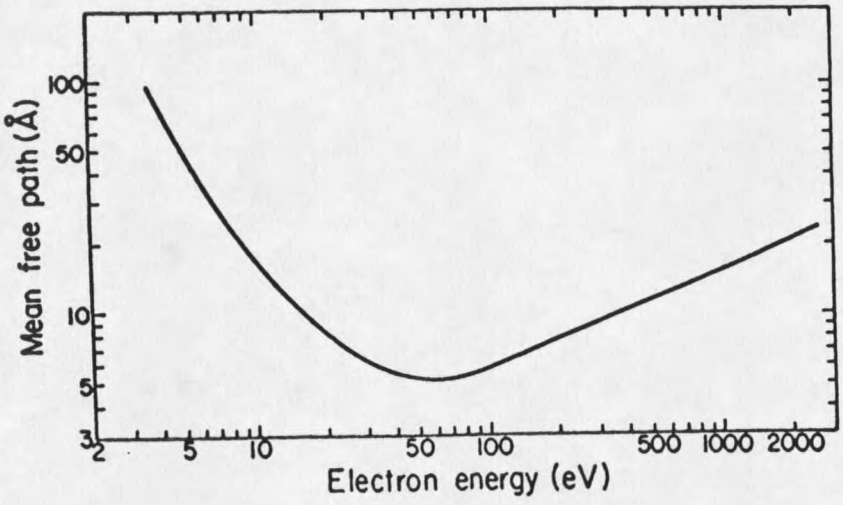


Fig. 11: "Universal Curve" of electron mean free path as a function of electron kinetic energy.

The damping of an electron wave can be fully described by $k'_i$. Thus, for a spherical wave, the wavefunction, $\Psi$, is

$$\begin{aligned}\Psi \sim \exp\,[i(k'_r + ik'_i)r] &= \exp\,(-k'_i r)\,\exp\,(ik'_r r) \\ &= \exp\,(-r/\lambda_{ee})\,\exp\,(ik'_r r)\end{aligned} \tag{3.13}$$

where the damping effect is represented by the mean free path $\lambda_{ee}$. It follows that

$$\lambda_{ee} = \frac{1}{k'_i} \tag{3.14}$$

For electron energies substantially larger than the magnitude of $V_{oi}$ one can relate this to $\lambda_{ee}$ through Equations (3.11) and (3.12)

$$\lambda_{ee} \approx 3.90\, E^{1/2}/V_{oi} \tag{3.15}$$

where E and $V_{oi}$ are expressed in eV and $\lambda_{ee}$ in Å. We can estimate that a value of $\lambda_{ee}$ of 10 Å at an energy of 100 eV corresponds to a value of $V_{oi}$ of 3.9 eV.

Thermal Vibration

The thermal motions of atoms reduce the intensities of the diffracted beams and increase the background.[41] The correction is made in LEED by an effective Debye-Waller factor $e^{-M}$ multiplying the scattering amplitude of each atom (given by t-matrix of Eq. (3.3)). The effective atomic scattering amplitude $t^T(\theta)$ can be expressed[24]

$$t^T(\theta) = e^{-M}\, t(\theta)$$

The calculation of Debye-Waller factor $e^{-M}$ can be found in Ref.[24]. Fortunately the structural results are affected by this factor only to a minor extent.

Multiple Scattering

We have discussed single atom scattering. In order to treat the scattering by a subplane, which contains identical atoms, we start from the two-atom scattering process, and consider multiple scattering path.

*Two-Atom Scattering*

Treating an incident wave as a plane wave, we use the spherical wave approximation to characterize the multiple scattering wave in the region between the atoms in the subplane. First we express how a spherical wave with angular momentum L'=($l$ ', m'), centered on the first atomic position $\mathbf{r}_1$, propagates to the second atomic position $\mathbf{r}_2$, and how this wave can be decomposed into spherical waves centered at $\mathbf{r}_2$. From wave propagation theory, which assumes a free field between two scattering positions, a Green's function of the following form describes the amplitude of a spherical wave L=($l$ , m) centered at the second atom due to a spherical wave centered on the first atom[24]

$$\overline{G}^{21}_{LL'}(k,\mathbf{r}_2-\mathbf{r}_1) = -4\pi i\frac{2m}{\hbar^2}k\sum_{L_1} i^{l\,1'}a(L,L',L_1)h^{(1)}_{l\,1}(k|\mathbf{r}_2-\mathbf{r}_1|)Y_{L_1}(\mathbf{r}_2-\mathbf{r}_1) \quad (3.16)$$

where $h_l^{(1)}$ is the Hankel function and $Y_L$ is a spherical harmonic. The angular momentum $L_1$=($l_1$,$m_1$) extends over all values of $|l-l'| \le l_1 \le |l+l'|$ and m+m'=$m_1$, and a(L,L',L1) is the Clebsch-Gordan coefficient or the so-called 3-j coefficient, with

$$a(L,L',L_1) = \int Y^*_L(\Omega)Y_{L'}(\Omega)Y^*_{L_1}(\Omega)d\Omega \quad (3.17)$$

where $\Omega$ ranges over all values of solid angle.

Consider the scattering path between two atoms. The t-matrix describes the amplitude of the scattering of a spherical wave with angular momentum L' by the first atom. The incident wave of the second atom with L generated by L' is described by the product $\overline{G}^{21}_{LL'}\cdot t^1_{l'}$. It is possible to combine such scattering events sequentially. Fig. 12 shows the scattering path for this sequence, where $t^1$ and $t^2$ are the respective t-matrices of

the first and second atoms. Table 2 expresses the amplitude for a succession of scattering events.

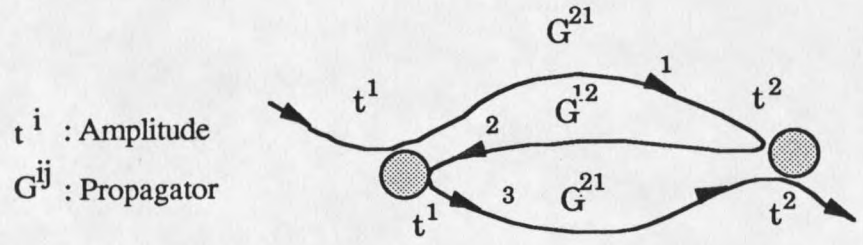


Fig. 12: Multiple scattering of a spherical wave by two atoms, showing Green's function notation.

TABLE 2. A succession of scattering for two atoms.

| # of scattering paths | atom 1 | | atom 2 | |
|---|---|---|---|---|
| | input wave | output wave | input wave | output wave |
| 1 | $t^1$ | $G^{21}t^1$ | $G^{21}t^1$ | $t^2G^{21}t^1$ |
| 2 | $t^2G^{21}t^1$ | $G^{12}t^2G^{21}t^1$ | $G^{12}t^2G^{21}t^1$ | $t^1G^{12}t^2G^{21}t^1$ |
| 3 | $t^1G^{12}t^2G^{21}t^1$ | $G^{21}t^1G^{12}t^2G^{21}t^1$ | $G^{21}t^1G^{12}t^2G^{21}t^1$ | $t^2G^{21}t^1G^{12}t^2G^{21}t^1$ |
| : | : | : | : | : |

The next step in the mathematical process is to construct a self-consistent form of the scattering amplitudes of all scattering paths that terminate at atom 1 and at atom 2, respectively, denoting these sums by $T^1$ and $T^2$

$$T^1 = t^1 + t^1G^{12}t^2 + t^1G^{12}t^2G^{21}t^1 + t^1G^{12}t^2G^{21}t^1G^{12}t^2 + \ldots$$
$$T^2 = t^2 + t^2G^{21}t^1 + t^2G^{12}t^1G^{12}t^2 + t^2G^{21}t^1G^{12}t^2G^{21}t^2 + \ldots \qquad (3.18)$$

If we assume the Green's function is independent of the source of LEED electrons, the above equation can be written as

$$\begin{aligned} T^1 &= t^1 + t^1 G^{12} T^2 \\ T^2 &= t^2 + t^2 G^{21} T^1 \end{aligned} \quad \text{or} \quad \begin{bmatrix} I & -t^1 G^{12} \\ -t^2 G^{21} & I \end{bmatrix} \begin{bmatrix} T^1 \\ T^2 \end{bmatrix} = \begin{bmatrix} t^1 \\ t^2 \end{bmatrix} \tag{3.19}$$

Where I is an unit matrix.

*N-Atoms Scattering*

It is straightforward to generalize the above results to a set of N atoms, located at positions $\mathbf{r}_1, \mathbf{r}_2, \ldots, \mathbf{r}_n$. The results will be generalized immediately as

$$\begin{bmatrix} I & -t^1 G^{12} & -t^1 G^{13} & \cdots & -t^1 G^{1N} \\ -t^2 G^{21} & I & -t^2 G^{23} & \cdots & -t^2 G^{2N} \\ -t^3 G^{31} & -t^3 G^{32} & I & \cdots & -t^3 G^{3N} \\ \vdots & \vdots & \vdots & \vdots & \vdots \\ -t^N G^{N1} & -t^N G^{N2} & -t^N G^{N3} & \cdots & I \end{bmatrix} \begin{bmatrix} T^1 \\ T^2 \\ T^3 \\ \vdots \\ T^N \end{bmatrix} = \begin{bmatrix} t^1 \\ t^2 \\ t^3 \\ \vdots \\ t^N \end{bmatrix} \tag{3.20}$$

*One-Subplane Scattering*

Let us consider a single plane of identical atoms that extends to infinity in all directions of the plane, with only one atom in each unit cell. Note that identical atoms have the same t-matrix, t. By symmetry, the diffraction of a spherical wave incident on any one of these atoms is identical to that of an identical spherical wave incident on any other atom. Consequently, if $T^i$ represents the scattering from atom i, then $T^1=T^2=....T^i=\tau$. Thus

$$\tau = t + t\left[\sum_i{}' \bar{G}^{in}\right]\tau \tag{3.21}$$

where i extends over all atoms. A new Green's function can be derived as

$$G^{sp}_{LL'}(k) = \sum_i{}' \bar{G}^{in}_{LL'} = -4\pi i \frac{2m}{\hbar^2} k \times \sum_{L_1} \sum_{\mathbf{P}}{}' i^{l\,1} a(L,L',L_1) h^{(1)}_{l\,1}(k|\mathbf{P}|) Y_{L_1}(\mathbf{P}) \exp(-\mathbf{k}\cdot\mathbf{P}) \tag{3.22}$$

Where **P** represents all atomic positions and extends over all atoms under consideration, except **P**=0.

*Scattering by N Subplanes.*

From the above formalism, a single atom may be characterized by the t-matrix determined by Equation (3.3), and a single subplane with identical atoms is characterized by the $\tau$-matrix given in Equation (3.21). The next step is to derive the multiple-scattering paths of N subplanes that have the same unit cell, but possibly different atoms. Let $\Gamma^i$ represent all multiple-scattering paths that terminate at an atom of plane i. Then $\Gamma^i$ can be considered to consist of two components: one for all paths internal to plane i, and another for paths that terminate at any atom of other planes and then extend to any atom in the i plane, where they may be treated by internal multiple paths. Therefore, a generalization to N-subplanes scattering is similar to the treatment of Equation (3.20):

$$\begin{bmatrix} I & -\tau^1 G^{12} & -\tau^1 G^{13} & \cdots & -\tau^1 G^{1N} \\ -\tau^2 G^{21} & I & -\tau^2 G^{23} & \cdots & -\tau^2 G^{2N} \\ -\tau^3 G^{31} & -\tau^3 G^{32} & I & \cdots & -\tau^3 G^{3N} \\ \vdots & \vdots & \vdots & \vdots & \vdots \\ -\tau^N G^{N1} & -\tau^N G^{N2} & -\tau^N G^{N3} & \cdots & I \end{bmatrix} \begin{bmatrix} \Gamma^1 \\ \Gamma^2 \\ \Gamma^3 \\ \vdots \\ \Gamma^N \end{bmatrix} = \begin{bmatrix} \tau^1 \\ \tau^2 \\ \tau^3 \\ \vdots \\ \tau^N \end{bmatrix} \tag{3.23}$$

with the new Green's functions,

$$G_{LL'}^{\lambda\lambda_1}(k,\mathbf{r}_\lambda - \mathbf{r}_{\lambda_1}) = -4\pi i \frac{2m}{\hbar^2} k \cdot \sum_{L_1} \sum_{\mathbf{P}}{}' i^{l_1} a(L,L',L_1) h_{l_1}^{(1)}(k|\mathbf{r}_\lambda - \mathbf{r}_{\lambda_1} + \mathbf{P}|) \cdot \cdot Y_{L_1}(\mathbf{r}_\lambda - \mathbf{r}_{\lambda_1} + \mathbf{P}) \cdot \exp[-\mathbf{k} \cdot (\mathbf{r}_\lambda - \mathbf{r}_{\lambda_1} + \mathbf{P})] \tag{3.24}$$

In this expression, $\mathbf{r}_\lambda$ and $\mathbf{r}_{\lambda 1}$ are atomic sites in planes $\lambda$ and $\lambda_1$, respectively, while $\mathbf{P}$ extends over the lattice points of any of the planes, except the point $\mathbf{r}_\lambda - \mathbf{r}_{\lambda 1} + \mathbf{p} = 0$. If we keep the incident plane wave $\exp(i\mathbf{k}_i \cdot \mathbf{r})$ used up to this point and wish to consider the amplitude of the outgoing plane wave $\exp(i\mathbf{k}_o \cdot \mathbf{r})$, it follows that the total scattering amplitude will be

$$\Gamma_{LL'} = \sum_{i=1}^{N} \exp[i(\mathbf{k}_i - \mathbf{k}_o) \cdot \mathbf{r}_i] \Gamma_{LL'}^i \tag{3.25}$$

## Duke and Laramore Method

Duke and Laramore extended the above theory and developed a method to describe multiple-interaction processes.[41] They first obtained a set of uncoupled integral equations for appropriately renormalized scattering amplitudes and then reduced the integral equations

to algebraic form. Their resulting expression for the scattering amplitudes is summarized by the following equations:

$$I(\mathbf{k}_o,\mathbf{k}_i;E_i) \sim \sum_{\lambda}\sum_{\mathbf{g}} \exp[-i(k_{o\perp}-k_{i\perp})d_\lambda - i\mathbf{g}\cdot\mathbf{a}]\Gamma_\lambda(\mathbf{k}_i,\mathbf{k}_o;E_i)\delta(k_{o\parallel}-k_{i\parallel}-\mathbf{g}) \qquad (3.26)$$

$$\Gamma_\lambda(\mathbf{k}_o,\mathbf{k}_i;E_i) = \tau_\lambda(\mathbf{k}_o,\mathbf{k}_i;E_i) + \sum_{\mathbf{k}}\sum_{\lambda_1\neq\lambda} \tau_\lambda(\mathbf{k}_o,\mathbf{k};E_i)G^{\lambda\lambda_1}(\mathbf{k},\mathbf{k}_i;E_i)\Gamma_{\lambda_1}(\mathbf{k},\mathbf{k}_i;E_i) \qquad (3.27)$$

$$\tau_\lambda(\mathbf{k}_o,\mathbf{k}_i;E_i) = t_\lambda(\mathbf{k}_o,\mathbf{k}_i;E_i) + \sum_{\mathbf{k}} t_\lambda(\mathbf{k}_o,\mathbf{k};E_i)G^{sp}(\mathbf{k},\mathbf{k}_i;E_i)\tau_\lambda(\mathbf{k},\mathbf{k}_i;E_i) \qquad (3.28)$$

In the above equations, $I(\mathbf{k}_o,\mathbf{k}_i;E_i)$ is the scattering amplitude, and the $\Gamma$, $\tau$, and t-matrices are defined as in Equations (3.25), (3.21), and (3.3). A particular value of the index $\lambda$ denotes a given subplane, while $\mathbf{g}$ is a vector in the reciprocal lattice of the subplane, $\mathbf{a}$ is a vector denoting the shift in the positions of the center atom between successive subplanes, and $d_\lambda$ is the perpendicular distance of the $\lambda$th subplane from the surface (i.e., $d_o$=0). The equations $G^{sp}$ and $G^{\lambda\lambda 1}$ are the subplane and interplane propagators defined by equations (3.22) and (3.24), respectively.

## From Theory to Computer Program

The physical processes outlined above exhibit the essential ingredients of all dynamical theories. An accurate computer program to calculate the LEED intensity curves should treat these processes. In fact, the program we used is organized in the same way the theory is organized. Every equation in the theory was implemented in a separate subroutine, e.g. the intra-plane and inter-plane propagators, the spherical harmonics, etc.

The phase shifts were calculated before the multiple scattering formalism was executed. In the next chapter the computer code will be described in more detail.

# CHAPTER 4

# COMPUTER PROGRAM

Dynamical LEED theory describes the phenomenon of electron wave propagation through an ordered surface, considered as a certain number of atomic layers. Any LEED computer code should reflect the phenomena discussed in the previous chapter. In this chapter, the basic features of the computer algorithms are discussed in terms of both the physical concepts and their mathematical treatment. Details of the organization and an outline of several subroutines are described.

## Description of Code

A new dynamical LEED computer code was written by our group at Montana State University, and is based on the subroutines originally developed by the group of C. Duke some 15 years ago;[41] in many cases extensive revisions have been made. The programs were written in standard Fortran in order to be accepted by compilers on most machines. Several significant extensions of the old code have been introduced. The program format was revised for the purpose of vectorizing the code; the old code was in scalar format optimized for the CDC 205 and could not easily be transported to other computer architectures. The new code can be run efficiently under a VAX 8550 cluster, CDC 205, ETA-10, and the Cray XMP. A generalized flowchart of the calculation process is presented in Fig. 13.

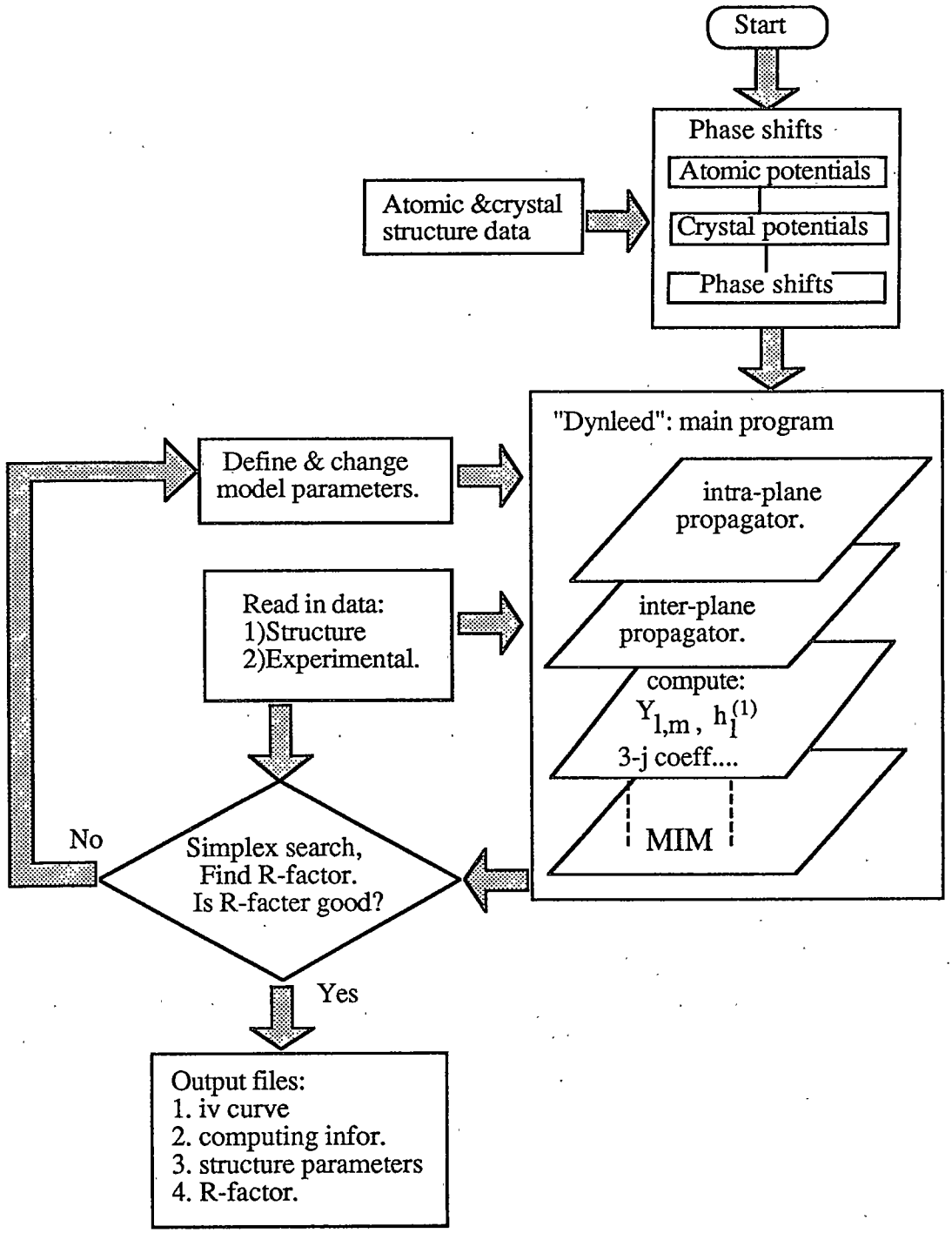


Fig.13: Generalized flowchart of dynamical LEED program.

As we pointed out in the previous chapter, the dynamical LEED theory consists of two main features. First, the electron scattering by individual atoms is taken in isolation and is treated by multiple scattering process, which is characterized by energy-dependent phase shifts; second, multiple scattering of the diffracting electrons among the atoms of the crystal surface is treated with various perturbation methods as described in chapter 5 and 6. Accordingly, a computer code should consist of two parts to treat these problems separately.

Phase Shift Calculation

Electron scattering by an individual atom in the surface under consideration is taken into account by assuming spherically symmetric interaction potentials surrounded by regions of constant potential (the muffin-tin model). The scattering is described using energy-dependent partial-wave phase shifts. In our computer code, each atomic scattering center is represented as a neutral atom. The first step in our method is the calculation of the atomic potentials by a self-consistent procedure. This step begins with the specification of an initial charge density and a potential energy derived from it. Then, through a relativistic Hartree-Fock-Slater muffin-tin model with an energy-dependent Hara exchange term, the electronic wave Equation (3.7) described in the previous chapter is solved. The resulting wave functions are used to calculate a new charge density and the above process is repeated until a convergence criterion is met, i.e. the potential and charge density are suitably consistent with each other.

The second step in the phase shift calculation is to obtain the crystal potential corresponding to overlapping atomic charge densities. The atomic potentials and an input data file, which specifies the geometry of the crystal and its atomic composition, are needed for this step. The bulk atomic charge densities are modified by superimposing the charge densities of the neighboring sixteen shells of atoms, assuming bulk coordination. The

adatoms are treated as free atoms and no superpositioning of neighboring charge densities is performed. Finally, the resulting effective-scattering potential is inserted into the radial Schrödinger Equation (3.7), which is integrated to yield the scattered wave phase shifts, as described in the previous chapter.

The program to calculate the phase shifts is call *xtalphase* . The input files include the atomic file and the crystal file. Atomic information includes: atomic shell, orbital function, an initial charge density, and the number of electrons in each state. Crystal information includes: lattice constant, atomic distances for sixteen atomic shells, and number of atoms per shell. The output file contains the phase shift data as a function of the incident electron energy. The energy range is 30~300 eV.

The phase shifts calculated from the potential model described above depend on the atomic species in the crystal. In the clean-surface case, if Si or Ge is the substrate, only one crystal potential is calculated; for binary compounds, i.e. GaAs, two separate crystal potentials are calculated. In the case of an overlayer system, another set of phase shifts, for the adatoms, is also needed.

Intensity Calculation: Main Program

This section presents some details of the main program and gives some guidelines as to which of the various possible calculational methods is most useful and what kind of values to give for input parameters in any given situation.

As illustrated in Fig. 13, the main program used to calculate the diffraction I-V curves for the surface under consideration is called *dynleed.* The input files to the main program must be prepared in advance: a) a phase-shift data file for each atomic species; b) a structure file, which is a data file that specifies the initial model geometry, energy range, beam indices, and inner potential, c) an initial file, which describes the model parameters, etc.. The trial structural model can be based on either theoretical considerations or data.

The perturbation treatment for surface atomic layer uses Matrix Inversion Method (MIM),[24] which solves the intensity matrix of Equation (3.23) for this slab.

Our source code can apply to two types of surface structures, rectangular and hexagonal. The old code used a two-sublattice formalism which applies only to a rather restricted class of surfaces; with it, only zincblende (110) surfaces can be analyzed. The cation and anion layers were treated as different sublattices in order to achieve a rectangular geometry. The extension was made by using one sublattice to reduce the structural constraints, thus providing more flexibility in calculating different geometries of the surface unit cell. The new version treats all atoms as the same type of lattice and differentiates them only through their phase shifts. In this fashion, different geometries of the surface unit cell can be treated; usually, small modifications are sufficient, as in rectangular, hexagonal, or square geometries. The input structure file contains the type of surface structure being chosen. In this thesis work, semiconductor silicon and germanium (111) surfaces are the chosen substrates, all of which exhibit hexagonal structure. The intra-plane and inter-plane propagators for the hexagonal structure were revised; these are needed in order to calculate the two-dimensional sums in hexagonal reciprocal space.

The main program shown in Fig. 13 is quite complicated. Before the algorithmic structure of *dynleed* is explained, the logical framework behind the program will be outlined. From a programming perspective, *dynleed* is a highly organized structure in which each specific task has its own dedicated subroutine. The subroutines that perform primary tasks are often invoked from several different places within the program, and so must consist of a collection of rules and functions that operate upon a general class of variables passed to them. The motivation for the establishment of generalized subroutines is apparent from the significant benefits thus derived for the programmer. Not only is redundancy avoided and program length minimized, but also debugging is made relatively straightforward when only one subroutine handles a single type of task. The structure of

the program follows the self-consistent formalism of the multiple scattering theory and its associated equations given in previous chapter. In those equations, the intraplane and interplane propagators, $G^{sp}$ and $G^{\lambda\lambda'}$, the spherical Hankel functions $h^{(1)}$, the Bessel functions $j_l$, the spherical harmonic functions, $Y_{l\,m}$, the Clebsch-Gordan coefficients, $a(L,L',L_1)$, etc. have to be computed in angular momentum space. Computations of those functions were performed in separate subroutines, which can be called regularly during an entire session by the main program.

The central task of the main program is the calculation of the layer diffraction matrices for: a) a single Bravais-lattice subplane, the amplitude of which is given by equations (3.22) and (3.23) (characterized by $\tau$-matrices). b) a composite layer, treated by the matrix-inversion method for the $\Gamma$-matrix of equations (3.24) and (3.25). The dimension of the $\Gamma$-matrix is determined in part by the number of layers treated exactly and the number of phase shifts; the computational time increases quite rapidly with these quantities. The perturbation treatment of the remaining subplanes proceeds by summing the single-subplane $\tau$-matrices. Finally, the total diffraction intensities were obtained by summing all contributions from the $\Gamma$-matrices and $\tau$-matrices.

Data Evaluation

The analysis of I-V curves to extract the surface geometry proceeded by comparing the experimental and calculated data. First, the diffraction intensities were calculated for the trial geometric model assumed to be responsible for the LEED pattern. Then these intensities were compared with the measured data, and the quality of fit was assessed by both visual and quantitative methods based on the reliability factor, or R-factor; the purpose of which is to satisfy the need for an objective criterion to compare theoretical and experimental curves. According to this trial-and-error approach, one makes intensity calculations for all plausible surface geometries and assumes that the one which gives the

best R-factor is the correct geometry. The R-factor we used in our program is the so-called x-ray R-factor, $R_x$ originally developed for use in x-ray crystallography.[51] The method compares experimental curve $I_{e,i}(E)$ and the calculated curve $I_{c,i}(E)$ for individual beam i, such that

$$r_i = \frac{\sum_E [I_{e,i}(E) - c_i I_{c,i}(E)]^2}{\sum_E [I_{e,i}(E)]^2} \tag{4.1}$$

where the summation is performed over the discrete energy value index, E. $c_i$ is a normalization constant defined by

$$c_i = \frac{\sum_E I_{e,i}(E) I_{c,i}(E)}{\sum_E [I_{c,i}(E)]^2} \tag{4.2}$$

Finally, adding in the results of several spectra and taking account of the beneficial effect of a large data set on reliability, an overall R-factor is defined by

$$R = [\frac{2}{3} + \frac{3}{2N}] \frac{\sum_{i=1}^{N} r_i \Delta E_i}{\sum_{i=1}^{N} \Delta E_i} \tag{4.3}$$

where N is the total number of beams incorporated, and $\Delta E_i$ is the energy range for the $i^{th}$ beam. This equation takes into account the beneficial effect of large data sets on reliability. Using this definition the range of significance of R values is evaluated from earlier

sensitivity analyses: $R_X$ values around 0.3 or perhaps a bit less be correspond to acceptable but probably not optimal structure, $R_X \leq 0.2$ suggest a 'good structure', and $R_X$ values greater that 0.3 are unacceptable.[52]

Several other aspects of the program are as follows. First, symmetry may exist in any particular application; for instance, the zincblende (110) surface has two-fold reflection symmetry. The exploitation of symmetry in the code can substantially reduce the computational effort. In the program, the intra-plane and inter-plane propagators require the calculation of two-dimensional lattice sums, which have been streamlined by performing symmetry-adapted summations. This symmetry incorporation was only made for the zincblende (110) face in the current code, which has (hk)=(-hk) reflection symmetry in the reciprocal lattice. In practice, this feature has allowed us to reduce the number of distinct unit cells used in the two-dimensional summations to 25 or less from 256 or more, with a concomitant savings in computer cost.

Simplex Algorithm

The method of varying the parameters in the search for a best- fit structure was based on the simplex algorithm.[53] With this method, the R-factor is used as a controlling factor in the search, and a set of structural and non-structural parameters are adjusted in a nonlocal search for the best fit between the calculated and measured I-V curves, achieved with the minimum R-factor. The simplex search was started with a given set of initial trial values for each parameter based on the proposed geometric model and systematically excludes the worst values until a convergence criterion is satisfied. Criteria for deciding how low an R-factor must be has been discussed by Duke.[52] Usually, each proposed structure was optimized from different initial sets of parameters to ensure that a structure was found that gave the absolute minimum R-factor. Upon iteration of the simplex

algorithm the spread in values of each parameter is reduced. The method and its advantages and disadvantages are discussed elsewhere.[54]

## The Code Testing

After the code was constructed, we performed tests to ensure proper execution of the program. The following tests of the program have been made. First, we tested the program for rectangular surface structures. The I-V curves for an artificial GaAs(110) surface with the same input file (number of layers, number of phase shifts, etc.) was calculated using two independent codes, the version using Duke's subroutine with a two-sublattice format, and the modified one using a one-sublattice format. The I-V curves were visually identical, thus validating the code for the rectangular case. In comparing the CPU times spent by the two versions, we did not see much difference, as expected since the dimension of the G-matrices remained the same.

Since the old version of the code was written for rectangular structures, no work has been done on the hexagonal structure using this program. Thus, we needed some other way to test the code. Tong's group has provided a package of LEED programs. By using Tong's program, Kawazu et al.[10] performed a LEED intensity analysis on the Si(111)-$\sqrt{3}\times\sqrt{3}$-Ga system and found the optimal geometric structure for this system. We used their best fit geometric coordinates as input structure to repeat the dynamical calculation by our program. The result was quite encouraging. Figure 14 shows the I-V curves from this calculation; all six low- index beams are in good agreement with those published in the earlier paper, and all the peaks are in similar positions.

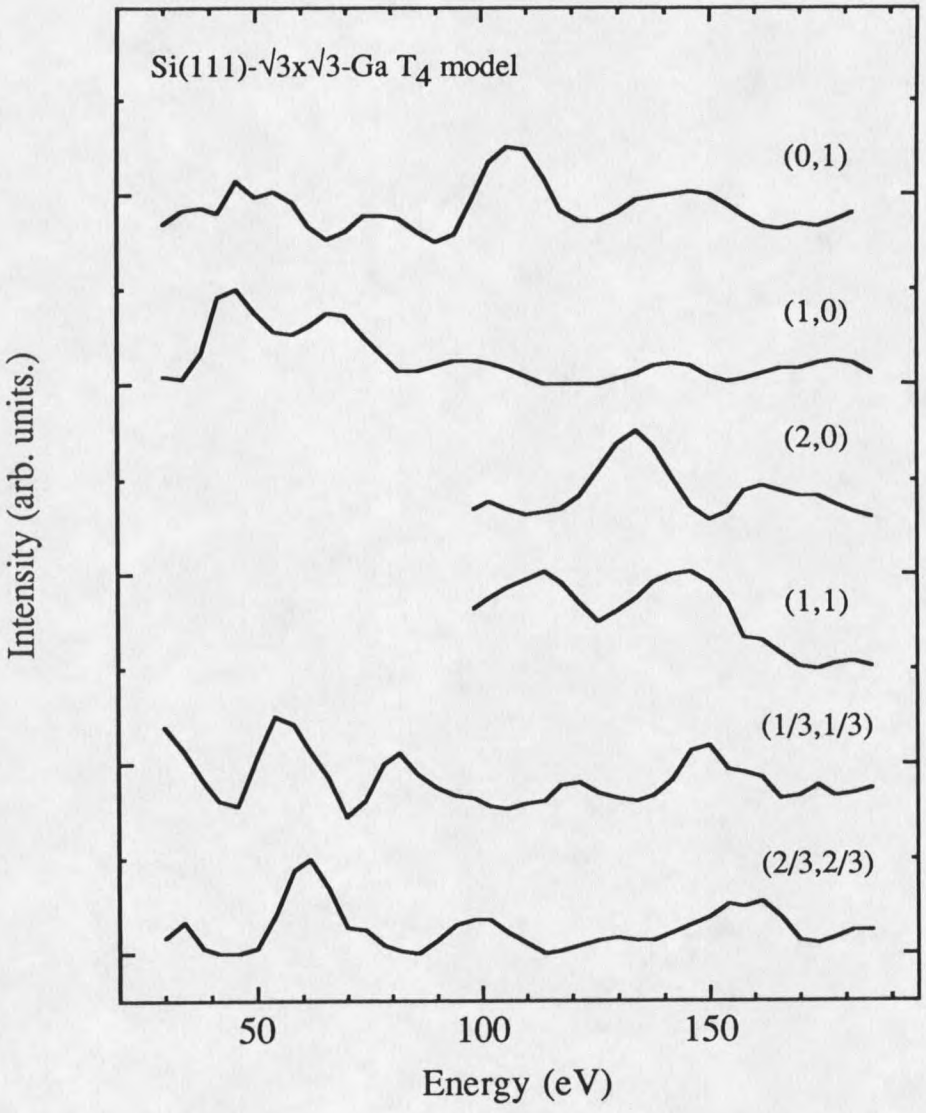


Fig. 14: I-V curves of the known Si(111)-$\sqrt{3}\times\sqrt{3}$- Ga structure calculated by current program. c.f. Ref.[10].

# CHAPTER 5

# GEOMETRIC STRUCTURES OF THIN BISMUTH AND ANTIMONY FILMS ON Si(111) SUBSTRATES

## Introduction

Antimony and bismuth adatoms induce ($\sqrt{3}\times\sqrt{3}$) structures on Si(111) substrates. For the Bi adatom, recent x-ray diffraction studies show that this ($\sqrt{3}\times\sqrt{3}$) structure appears at one monolayer coverage and 335 °C substrate temperature, in disagreement with the model of 1/3 ML saturated coverage proposed earlier by Kawazu from thermal desorption experiments.[55] However, the x-ray diffraction results are ambiguous in determining the orientation of the Si(111) surface in the sense that a 180° rotation about the normal leaves the data unchanged.[56] In the trimer model, the center of the trimer could be located at either the $T_4$ site or the $H_3$ site.

For the Sb adlayer, the ($\sqrt{3}\times\sqrt{3}$) reconstruction takes place at 670 °C at 1 ML coverage; a trimer model has been invoked to describe the structure. It has not yet been determined where the adatoms are bonded to the substrate or whether the Si substrate is reconstructed. Additional information is required to determine the true surface structure on an atomic scale.

In this chapter, we present the results of LEED investigation of the structure of the Bi/Si(111) and Sb/Si(111) systems. The experimental details described here are similar to those involved in the studies of Ge substrates in the next chapter.

## Experimental Details

Measurements

The experiments were performed in an UHV system with a base pressure of $8\times10^{-11}$ torr, the clean surface was obtained by the method described in chapter 2. We note that the annealing time and a slow cooling rate are important conditions for obtaining a clean (7×7) surface. Short annealing and rapid cooling result in the new ($\sqrt{3}\times\sqrt{3}$) reconstruction[57]. This new reconstruction on the Si(111) surface was observed during our experiment and confirmed by comparing the I-V curves with data from Fan et al.[57]

Our studies were made using LEED and Auger spectroscopy, via the retarding field analyzer method, using the experimental conditions described previously. Each ordered film studied displayed the three-fold symmetry of the (111) surface. This fact was utilized to infer the incident geometry of the LEED beam as discussed in chapter 2. The LEED diffraction patterns were integrated, digitized, and stored within the computer. I-V curves were accumulated and summed under computer control for typically thirty-two video frames before the spot intensities were analyzed. A typical 250 eV scan range at 2 eV increments for twelve or more beams took about five minutes. The symmetry-specific spectra were averaged among themselves prior to analysis. In order to increase the signal-to-noise ratio, three independent sets of data were recorded and the corresponding data sets were averaged and normalized to the beam current. I-V curves used for analysis were taken after the samples were cooled to ~ -120 °C to reduce effects due to lattice vibration.

The Auger spectra were measured as a function of the adlayer coverages and the annealing temperature. The data showed that an incident electron beam with an energy of 2 keV is capable of damaging the ordering of the sample and causing contamination of the surface during the Auger measurements. This contamination is probably due to the

desorbed gas from the chamber wall caused by the high energy electron bombardment. Therefore, separate samples were used to do the Auger measurements for different coverages and temperatures.

To illustrate how the (7×7) and the ($\sqrt{3}\times\sqrt{3}$) surfaces appear in our data, Figs. 15 and 16 present the experimental LEED images of those surfaces. Figure 15 was taken at an incident electron energy of 35.6 eV after the sample had been cleaned using the procedures described in chapter 2, while Fig. 16 was obtained at 45.1 eV following the deposition of 2 ML Bi on a 360 °C (7×7)-Si(111) surface.

Beam Index Convention

The beam index convention we adopted is the same as that used elsewhere.[58] Because the Si (111) surface forms hexagonal unit cells, and the bulk crystal structure of Si has threefold symmetry about the [111] axis, the diffraction pattern has threefold symmetry when the electron beam is incident normal to the surface, since the diffraction involves the bulk. In k-space, two of the three symmetry axes, labeled k-k' and h-h', can be chosen as the coordinate axes for the independent beams. This convention is illustrated in Fig. 17. Typically, we measured I-V curves for five integral-order beams ((1 0), (0,1), (2 0), (1 1), (0 2)) and four fractional-order beams((1/3 1/3), (2/3 2/3), (1/3 4/3), and (4/3 1/3) ). These beams comprised most of the independent low-index beams which could been seen on the screen over an energy range of 40 to 300 eV.

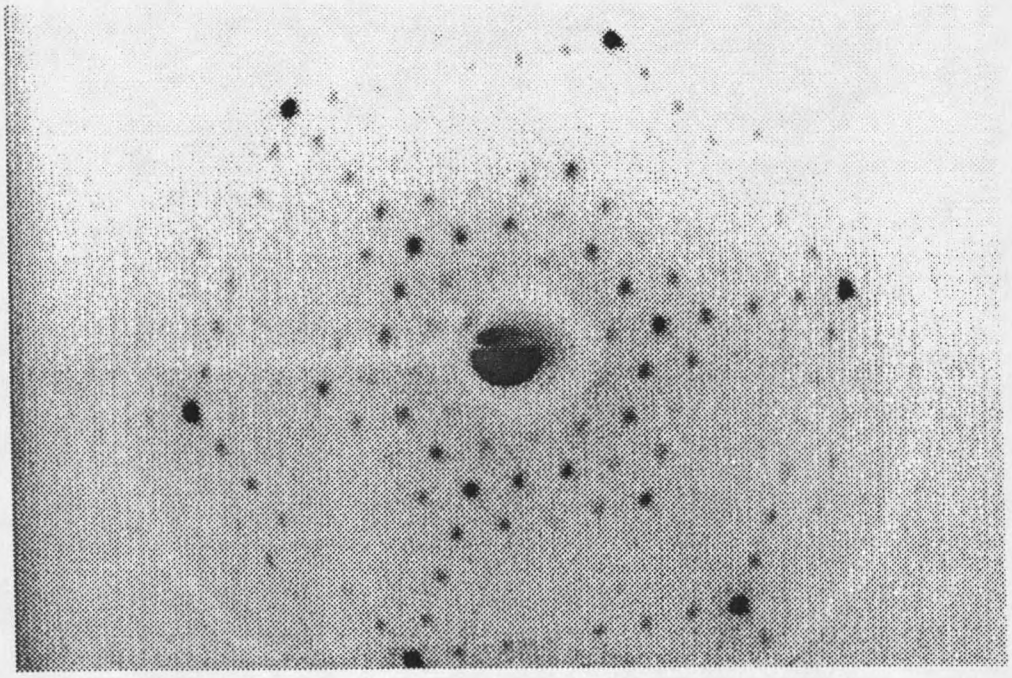

Fig.15: The LEED image of Si(111) 7×7 clean surface,taken at 35.6 eV.

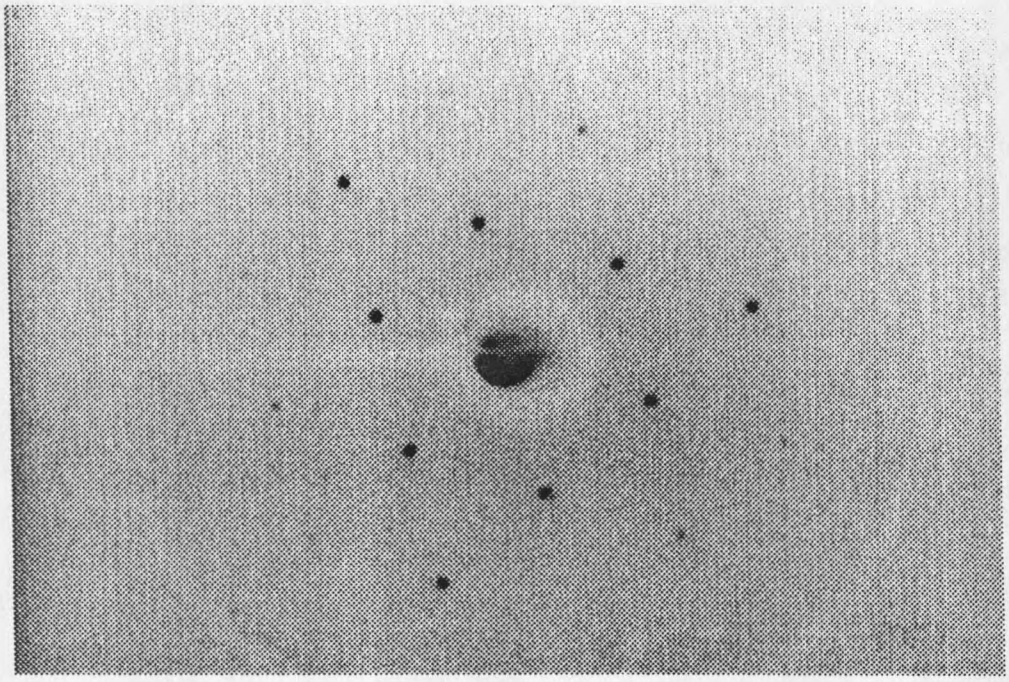

Fig.16: The LEED image of Si(111)-$\sqrt{3}\times\sqrt{3}$-Bi surface, taken at 45.1 eV.

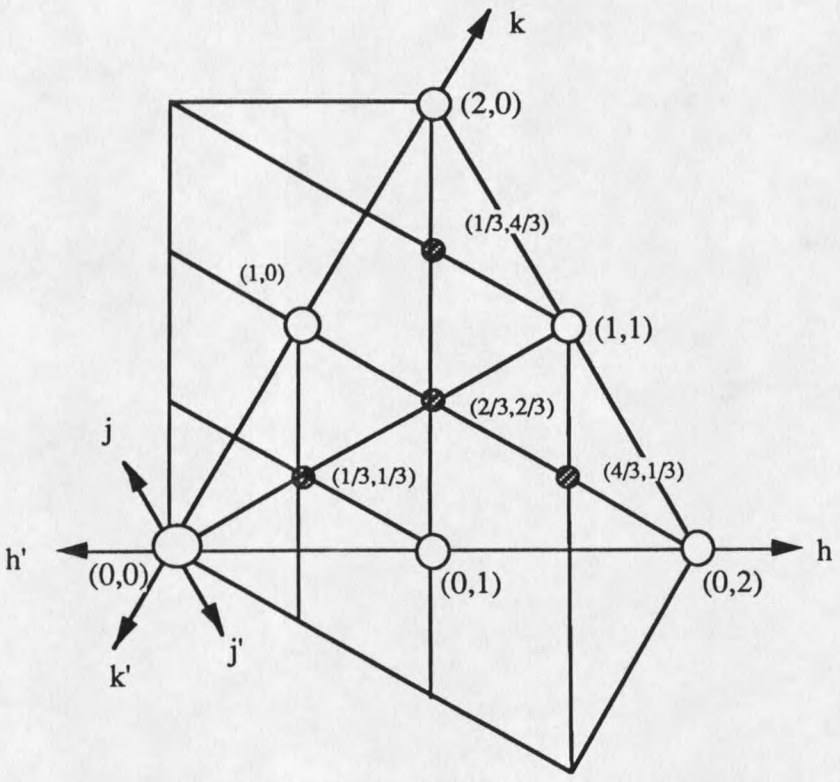


Fig.17: Beam notations in k-space for the Si(111)-($\sqrt{3}$x$\sqrt{3}$)-Bi surface. k-k', h-h', and j-j' are symmetry axes.

Incident Electron Beam Alignment

The incident electron beam was aligned within ~0.5° of the sample normal as permitted by our instrument.[37] The alignment procedure was described in our previous work.[59] This alignment matches the intensity curves of the symmetry-equivalent beams, e.g. (0 1)=(1 -1)=(-1 0); (1 0)=(0 -1)=(-1 1). Fig. 18 shows original I-V curves of the above six lowest-index integral-order beams (i.e. (0 1), (1 0), (1-1), (0-1), (-10), and

(-11)) obtained from (a) the clean surface and (b) a Bi-covered Si(111)-$\sqrt{3}\times\sqrt{3}$ surface, both sets of the I-V curves exhibit the 3-fold symmetry.

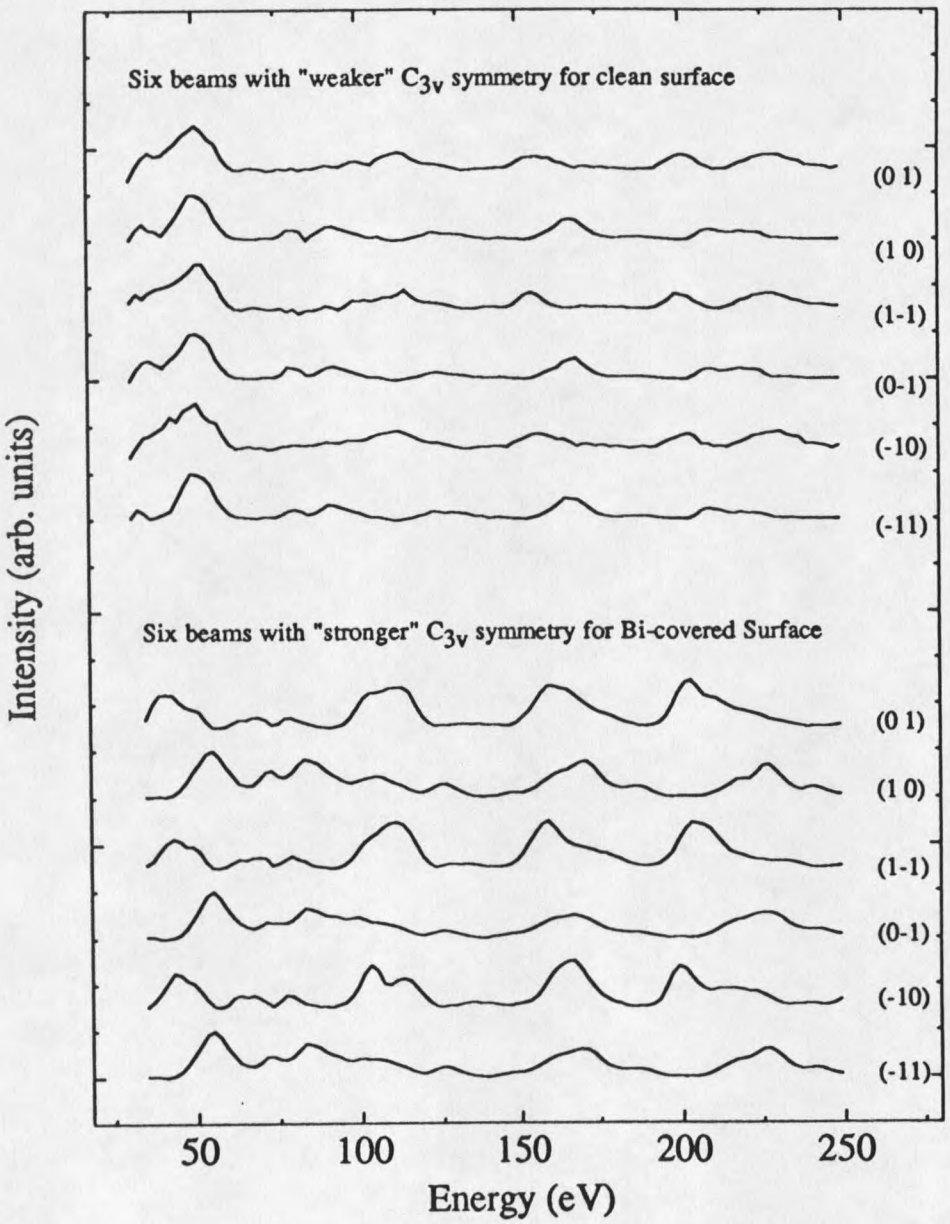


Fig.18: Illustration of symmetry relationships for six lowest integral-order beams.

## The Studies of Bi/Si(111) System

Experimental Results

The Si(111)-$\sqrt{3}\times\sqrt{3}$-Bi system proved to consist of two stable adsorption phases: We call them the $\alpha$ and the $\beta$ phases. The $\alpha$-phase structure corresponding to 1/3 ML bismuth adsorbed on the clean substrate at ~360 °C, and a $\beta$-phase structure corresponding to 1 ML bismuth adsorbed on the clean substrate at ~300 °C. Both structures displayed a $(\sqrt{3}\times\sqrt{3})$ superlattice. These conclusions can be justified by noting the Bi-coverage dependence and the temperature dependence of the structure as described next. The Bi overlayer was investigated by a qualitative examination of the diffraction intensities and a quantitative examination of the I-V curves as a function of Bi coverage, with the substrate kept at room temperature. For low coverages, a (7×7) pattern remained, with a background that increased beyond a coverage of 1/3 ML. A weak (1×1) pattern was observed up to 1 ML. Coverage more than approximately 1 ML removed the LEED pattern. The measurements of I-V curves revealed no essential change except for the background as the coverage increased. In Fig. 19 the I-V curves for the (1 0) diffraction spot are plotted. The results for a range of bismuth coverages from 0 to 2 ML are presented. The films used for this set of measurements were prepared and measured after a background contribution attributed to incoherent scattering had been subtracted out. These data are representative of the changes incurred by all of the diffraction beams we observed. The above observations indicate that the Bi overlayer is disordered both above and below monolayer coverage. Apparently, no overlayer reconstruction is obtained without thermal annealing.

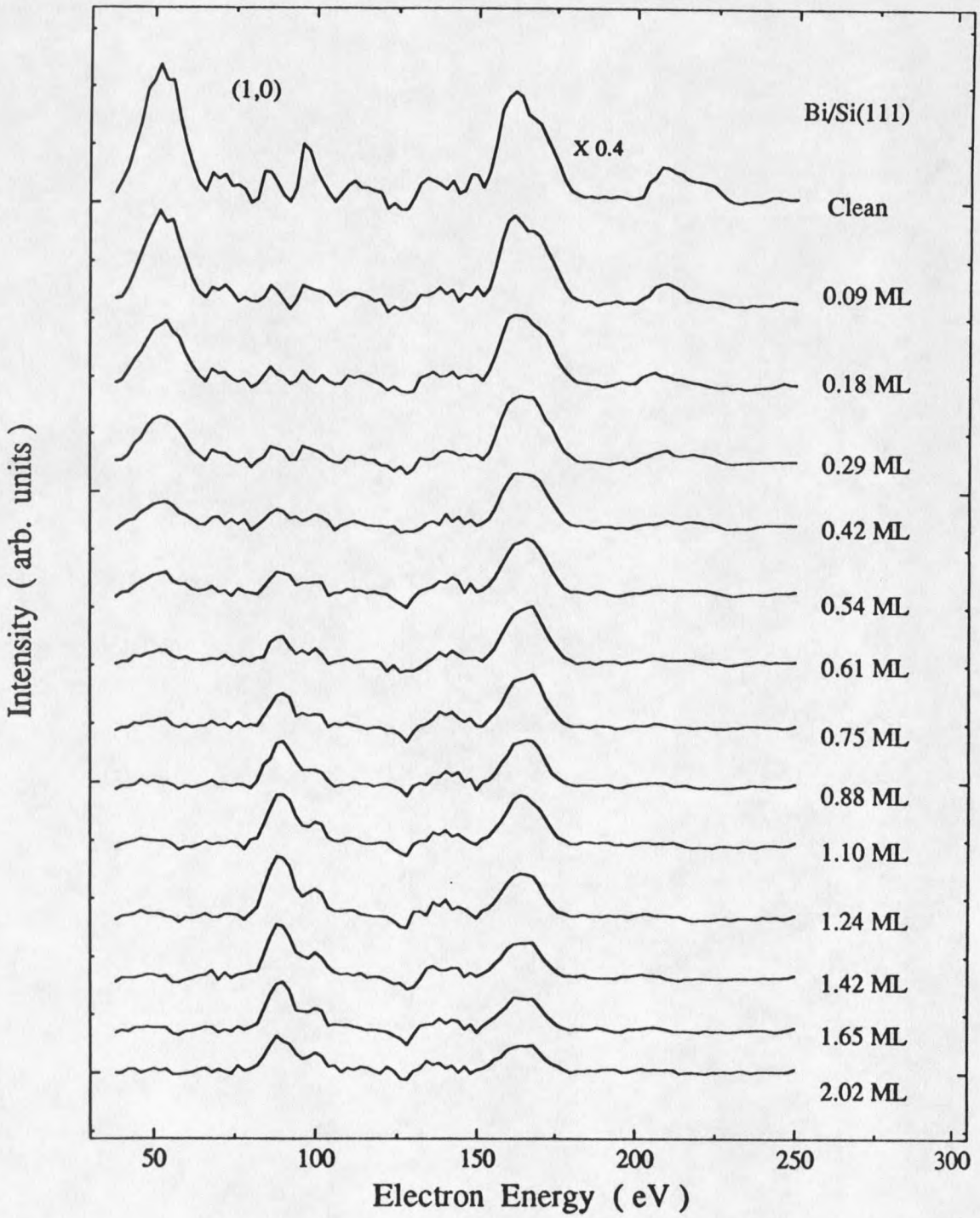


Fig. 19: Dependence of (1,0) beam intensity on Bi coverage for Bi/Si(111).

The production of different reconstructions requires starting from an annealed Si(111)-7×7 surface, and, in most cases, thermal annealing after deposition. Thus, the annealing temperature of a bismuth-covered surface was carefully monitored and controlled. The overlayer was produced by depositing 3 ML bismuth on a clean Si(111)-7×7 substrate kept at room temperature. The (7×7) pattern initially changes to a (1×1) pattern accompanied by an increased background. The annealing temperature was increased from room temperature to about 500 °C, where the Bi is believed to be desorbed. For every increment of 20 °C and 2 min., the sample was cooled to room temperature and the LEED pattern was recorded and I-V spectra were measured. When the annealing temperature exceeded 220 °C, a ($\sqrt{3}\times\sqrt{3}$) LEED pattern began to appear. At about 300 °C, the ($\sqrt{3}\times\sqrt{3}$) pattern appeared very clearly. However, upon further annealing in the range of 300~360 °C, the intensity of LEED spots decreased slightly and, surprisingly, became very clear again above 360 °C, with quantitatively different features, indicating that two different structures might be involved. Auger measurements indicated the Bi coverage at those two points was about 1 ML and 1/3 ML, respectively.

To confirm that two different phases exist in this system, the following sample preparations were made to determine the saturated bismuth coverage corresponding to the substrate temperature:

(i) (1, 2, 3)-ML bismuth films were deposited successively on a clean (7×7) room temperature substrate, followed by annealing to about 300 °C.

(ii) (1/2, 1, 2)-ML bismuth films were deposited successively on a clean room temperature substrate, followed by annealing to about 360 °C.

(iii) A 3-ML Bi film was deposited on a clean substrate kept at 300 °C.

(iv) A 2-ML Bi film was deposited on a clean substrate kept at 360 °C.

The observations of LEED patterns and the measurements of I-V curves for each sample prepared above confirmed our previous conjectures of two different phases

coexisted. For the first and second samples, the initial (7×7) pattern of the clean substrate was replaced by a weak, diffuse (1×1) pattern. Annealing reduced the background while the ($\sqrt{3}\times\sqrt{3}$) pattern started to appear at ~220 °C and got sharper at 300 °C. Additional annealing caused the background to increase; the sharp ($\sqrt{3}\times\sqrt{3}$) pattern reappeared at ~360 °C. For the third and fourth samples, the LEED patterns exhibited sharp ($\sqrt{3}\times\sqrt{3}$) symmetries, but each sample yielded different I-V curves. The LEED pattern from the fourth sample appeared brighter and the intensity of the beams was increased by a factor of ~2.7 compared with the second sample. This comparison indicates that the ($\sqrt{3}\times\sqrt{3}$) surface obtained by deposition on the hot substrate produced a better-ordered structure than did the surface prepared by room temperature deposition even when followed by annealing. Experiments showed that deposition with the substrate temperature between 300~360 °C also produced the ($\sqrt{3}\times\sqrt{3}$) LEED pattern, but the intensities of the extra spots were slightly weaker. When the substrate was heated above 450 °C, for each sample preparation, impinging bismuth atoms were re-evaporated, so no film growth was observed. The LEED pattern exhibited a (1×1) structure with I-V curves similar to those observed for the integral-order spots of the clean surface.

The I-V curves for all beams observed on the computer screen were measured when the sample was cooled down to ~-125 °C, to reduce thermal atomic vibrations. Figure 20 shows the I-V curves of the β-phase obtained from the third sample. The I-V curves from the fourth sample are qualitatively different from those of the α-phase structure as illustrated in Fig. 21. The data are grouped according to integral- and fractional-order beams. The two sets of spectra have distinctly different features.

The α and β-phases can also be observed in the first and second samples. Fig. 22(a) and 22(b) show the I-V curves for the (1 0) and (1/3 1/3) beams from each sample in the β-phase. Those two beams are representative of all the diffraction beams observed. Apparently the method of sample preparation plays an insignificant role. The same result

has been obtained for the α-phase. We find that the ($\sqrt{3}\times\sqrt{3}$) structure achieved by deposition on the hot substrate gives better stability and reproducibility for both the α-phase and β-phase; accordingly, we have used these data for the multiple-scattering analysis.

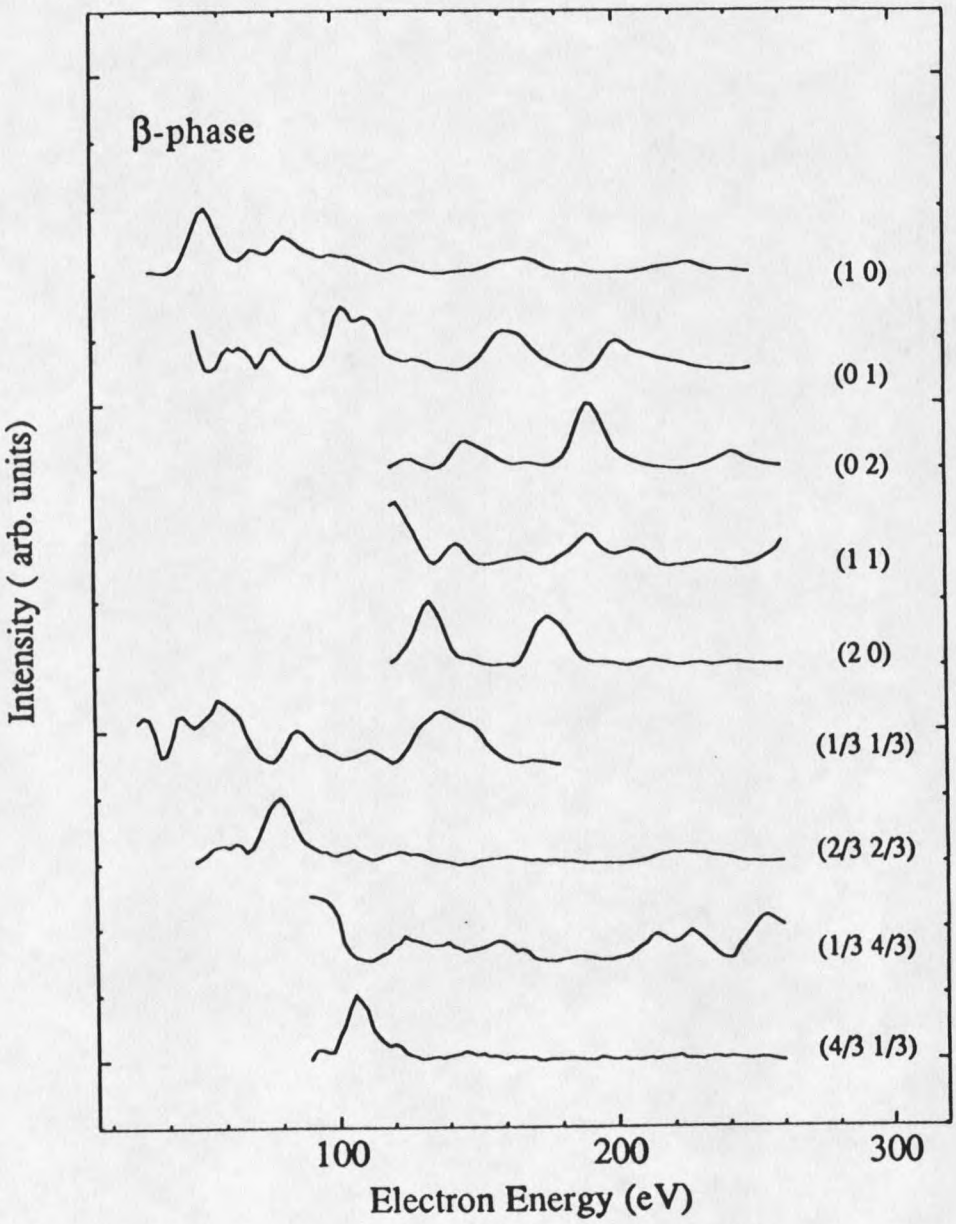


Fig.20: The I-V curves for the β-phase.

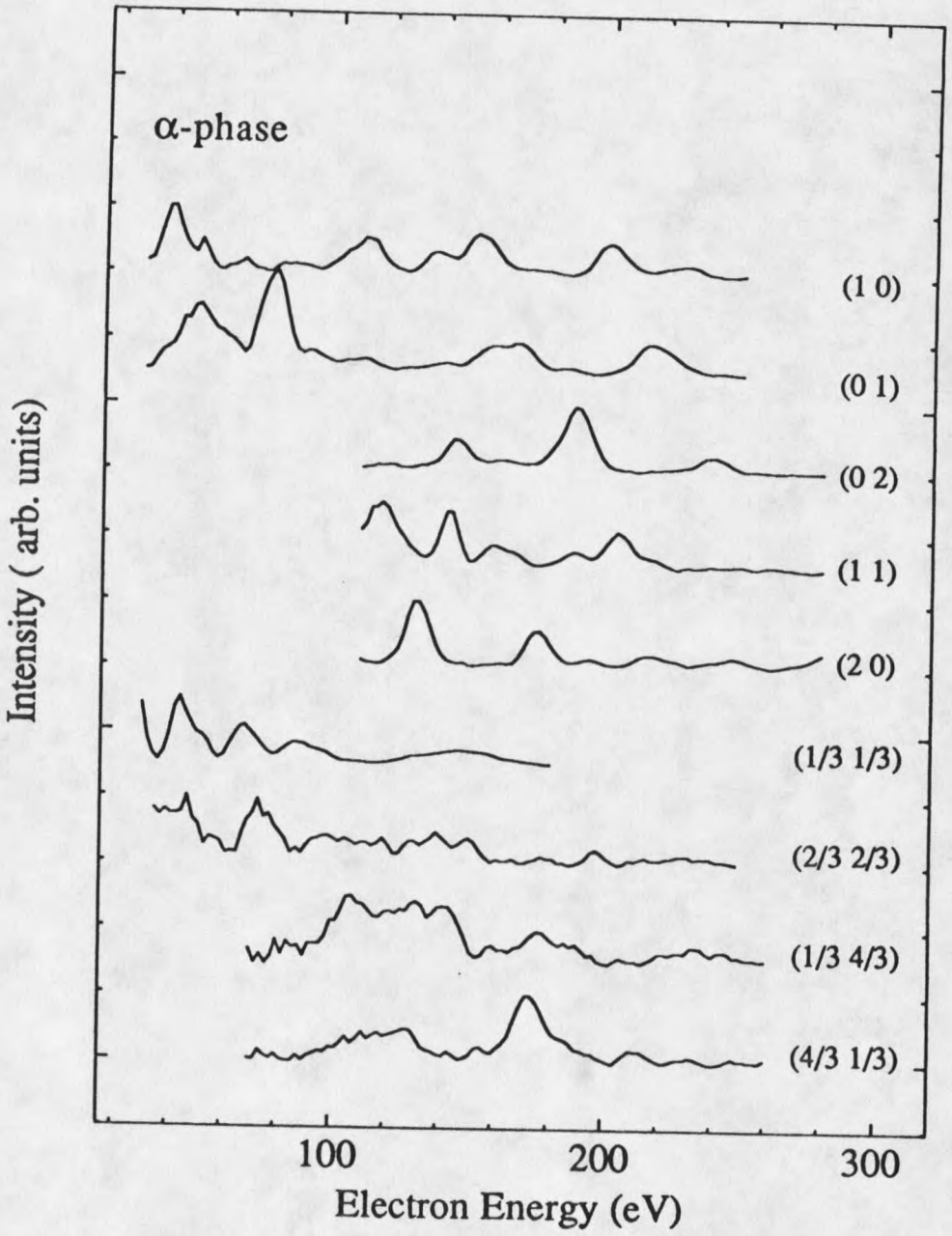


Fig.21 The I-V curves for the α-phase.

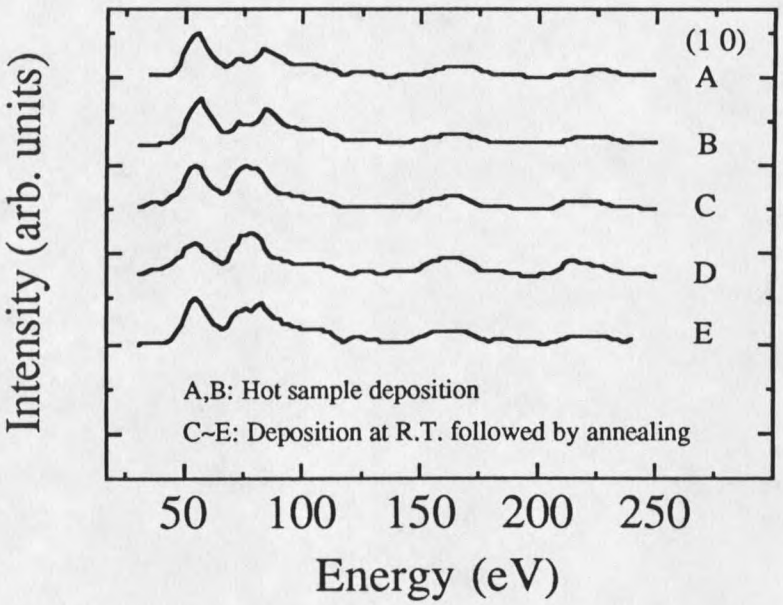


(a)

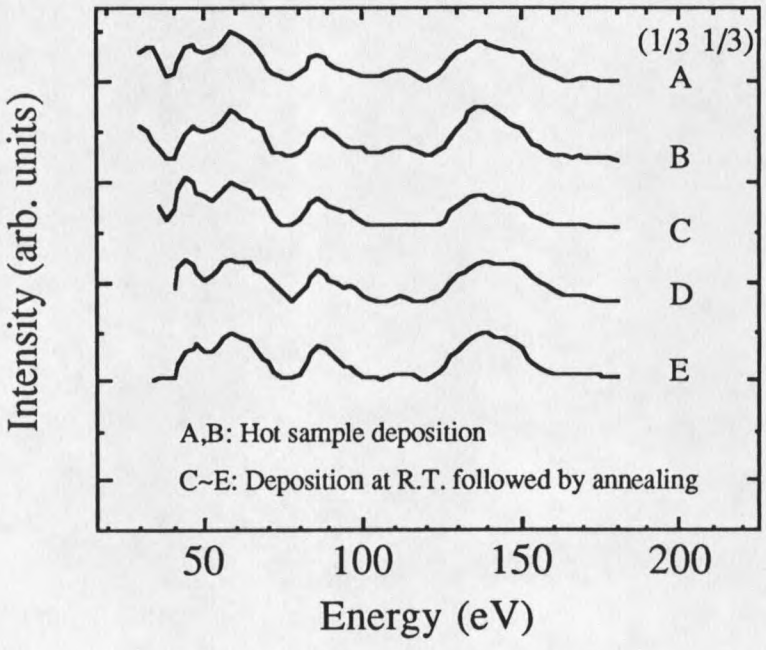


(b)

Fig.22: (a) (1 0) and (b) (1/3 1/3) Beam I-V curves; comparison of different sample preparations.

By measuring the Auger spectrum of these surface structures, we can determine the Bi coverages for both the α-phase and β-phase. Figure 23. shows the Auger measurement results for the above samples. The Auger line intensity was calibrated for a 1-ML film by using a quartz crystal oscillator. For each case, a bismuth coverage larger than 1 ML was deposited onto a clean (7×7) surface, and thermal annealing yielded the ($\sqrt{3}\times\sqrt{3}$) structure. At about 200 °C annealing temperature, the ($\sqrt{3}\times\sqrt{3}$) pattern was present along with a diffuse background. Up to ~300 °C annealing temperature, a sharp ($\sqrt{3}\times\sqrt{3}$) pattern was obtained. Apparently, some of the Bi desorbs from the surface, leaving a coverage of nearly 1 ML. Further annealing up to ~360 °C, caused more Bi atoms to be desorbed, until only about 1/3 of an atomic monolayer remained on the substrate. The observed behavior indicates that the α-phase can be transformed to the β-phase: from data on a 3-ML Bi adlayer at room temperature, we found that the α-phase can be obtained by thermal annealing to ~ 300 °C, and the β-phase can be obtained simply by continued annealing up to ~ 360 °C. The intensities of the LEED spots increased by a factor of about 2.5 when a temperature of 360 °C was reached. Thus we conclude that the bismuth coverages are 1/3 ML and 1 ML, for the α-phase and β-phase, respectively. For the third and fourth samples, Auger measurements indicated that 1 ML and 1/3 ML of Bi remain on the surface, as we indicated above.

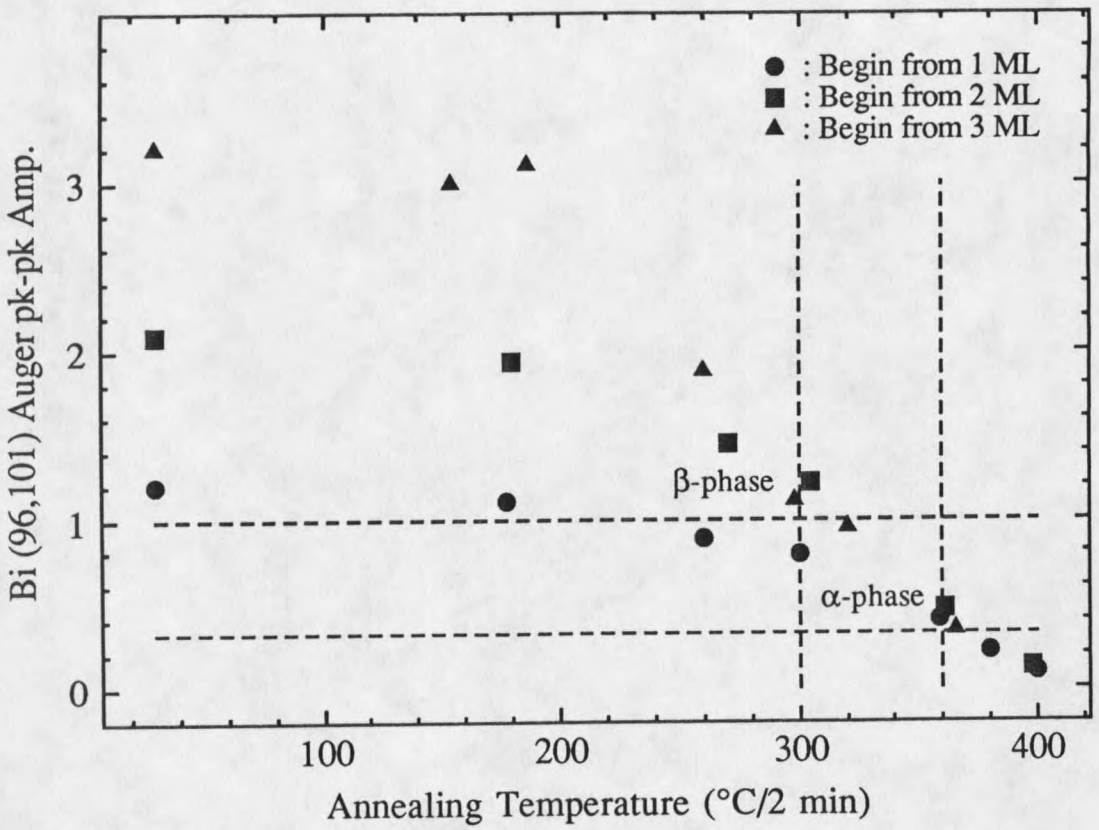


Fig.23: Bi (96 and 101 eV) Auger line intensity vs annealing temperature for 1.5 ML coverage on a Si(111) surface.

Discussion of Data

On the basis of the LEED and Auger data, it has been found that there are in fact two phases with the $(\sqrt{3}\times\sqrt{3})$ structure. The bismuth coverage depends on the substrate temperature. The saturation Bi coverages are 1 ML at ~ 300 °C and 1/3 ML at ~ 360 °C. The following conclusions can be drawn:

(i) The I-V curves from the first and third samples of above section are essentially identical, as are those form the second and fourth sample.

(ii) Each phase has a unique saturation coverage. As long as the substrate remains at the specified temperature, only 1/3 and 1 ML Bi coverage can remain on the surface, regardless

of the exposure; excess atoms are desorbed from the hot substrate. This behavior is consistent with the results of thermal desorption experiments by Kawazu et al,[55] although their observed temperature dependence is somewhat different from ours. They observed a dip in the desorption flux of Bi when the substrate was at ~ 460 °C , and a plateau between the 250 and 300 °C.

(iii) The phases of the two $\sqrt{3}$ structures are stable and reproducible. Small changes in the coverage and the substrate temperature affect only the intensity of each beam, while the major features of the I-V curves are essentially unchanged.

(iv) The β-phase structure, corresponding to 1-ML Bi coverage at 300 °C substrate temperature, can be transformed to the α-phase of 1/3 monolayer Bi at higher temperatures as bismuth adatoms are desorbed from surface.

(v) The intensities of LEED spots have turning points as a function of the annealing temperature, for the first and second samples. When the temperature exceeds ~300 °C or ~360 °C the intensities of beams increase markedly.

Next we discuss the atomic models proposed for each phase. Complete elucidation of the surface atomic structure requires detailed theoretical calculations, for which an especially powerful technique is provided by dynamical LEED theory. This calculation begins with a proposed structural model. So far, the trimer model for 1 ML adatom coverage and the $T_4$, $H_3$ models for 1/3-ML coverage have been suggested. From the data alone, it is not possible to conclude where the trimers are located on the substrate or whether the $T_4$ or $H_3$ model represents the correct geometry. Still, it is of interest to discuss a plausible symmetry of the $(\sqrt{3}\times\sqrt{3})$-Bi surface based on the experimental results before considering the theoretical analysis.

Because the Si(111) surface has $C_{3v}$ symmetry about the [111] axis, the diffraction beams should exhibit the same symmetry when the electron beam is incident normal to the surface. For the bulk-terminated surface, three-fold symmetry is ascribed to the presence

of second-layer Si atoms. When Bi is adsorbed on the substrate, the symmetry of the surface clearly must reflect the location of the adatoms by definition. As seen from Fig. 18, six low-index beams display threefold symmetry for both (a) the clean (7×7) surface and (b) the 1-ML bismuth-covered ($\sqrt{3}\times\sqrt{3}$) surface. Since there is no ambiguity in the substrate orientation in the LEED with respect to a 180° rotation, due to the rapid attenuation of the diffraction wave field inside the crystal, we can easily distinguish the (0 1) and (1 0) beams.[49] By symmetry, the (0 1), (1 -1) and (-1 0) are identical as are the (1 0), (0 -1) and (-1 1). For the clean-surface data shown in Fig. 18(a), the I-V curves show essentially six-fold symmetry because of the small penetration depth at low energy. At higher energy, when the incident electron beam penetrates deeper into the surface, the second Si layer contributes to the diffraction, leading to the occurrence of threefold symmetry. For a Bi-covered surface, the I-V curves shown in Fig. 18(b) display an even stronger threefold symmetry throughout the entire energy range. This implies that Bi atoms are located at special adsorption sites on the Si substrate that enhance the three-fold symmetry. If we consider either the $T_4$ or $H_3$ models as defined in chapter 1 for the α-phase, the symmetry information we obtained tends to favor the $T_4$ over the $H_3$ model. The reason is this: If the adatoms were located at the $T_4$ site, we would expect an enhancement of the threefold symmetry of the diffraction pattern compared with the clean surface, whereas the diffraction from an adatom located at an $H_3$ would counteract the contribution from second-layer Si atoms, leading to stronger six-fold symmetry. In the same way, for the β-phase , we infer that the trimers are centered above the second-layer Si atoms; i.e., at $T_4$ sites.

Dynamical Calculation

Dynamical LEED calculations of I-V curves for the Bi-Si(111)-$\sqrt{3}\times\sqrt{3}$ superstructure were performed to determine the atomic configurations responsible for each

phase. In this approach the structural and non-structural parameters are adjusted in a non-local search for the best fit between calculated and measured I-V curves.[59]

Electron scattering by surface atoms is described using energy-dependent phase shifts obtained from a bulk-Si superposition potential as described in chapters 3 and 4. The adsorbate Bi atoms are treated as free atoms - no superposition is carried out. The energy-dependent phase shifts associated with the above potentials are plotted in Fig. 24 (a)-(d). The phase shifts for a Ge substrate and an Sb adsorbate are also given in the figure; these are treated in the same fashion and will be used in the next chapter. The corresponding total elastic cross-sections computed using these phase shifts are presented in Fig. 25. Since Bi adsorbates have large scattering cross sections, more phase shifts are needed to achieve sufficient accuracy. However, because computing time increases very rapidly with the number of phase shifts used, and since convergence tests revealed that six phase shifts yielded intensities accurate to within a few percent,[60] we omitted higher phase shifts in the calculations. We assumed that all the inelastic processes due to the electron-electron interaction can be incorporated into the inelastic mean free path, $\lambda_{ee}$, and since it is energy-dependent and layer-dependent, we selected it to minimize the x-ray R factor, $R_x$. The consequences of thermal lattice vibrations are neglected in the structure search, because bulk lattice vibrations are not expected to be important in the analysis of I-V curves taken at temperatures well below the Debye temperature,[61] which is approximately 647 K at 77 K in the case of Si.